



1    **The interactive global fire module pyrE**

2    Keren Mezuman<sup>1,2</sup>, Konstantinos Tsigaridis<sup>1,2</sup>, Gregory Faluvegi<sup>1,2</sup>, Susanne E. Bauer<sup>2,1</sup>

3    <sup>1</sup> Center for Climate Systems Research, Columbia University, New York, NY, USA

4    <sup>2</sup> NASA Goddard Institute for Space Studies, New York, NY, USA

5    *Correspondence to:* Susanne E. Bauer ([Susanne.Bauer@columbia.edu](mailto:Susanne.Bauer@columbia.edu))

6

7

8

9

10

11

12

13

14

15

16

17

18

19

20

21

22

23

24

25

26

27

28

29

30

31



**Abstract.** Fires affect the composition of the atmosphere and Earth's radiation balance by emitting a suite of reactive gases and particles. An interactive fire module in an Earth System Model (ESM) allows us to study the natural and anthropogenic drivers, feedbacks, and interactions of open fires. To do so, we have developed pyrE, the NASA GISS interactive fire emissions module. The pyrE module is driven by environmental variables like flammability and cloud-to-ground lightning, calculated by the GISS ModelE ESM, and parameterized anthropogenic impacts based on population density data. Fire emissions are generated from the actual flaming phase in pyrE (fire count), not the scar left behind (burned area), as is commonly done in other interactive fire modules. Using pyrE, we examine fire behavior, regional fire suppression, burned area, fire emissions, and how it all affects atmospheric composition. To do so, we evaluate pyrE by comparing it to satellite-based datasets of fire count, burned area, fire emissions, and aerosol optical depth (AOD). We demonstrate pyrE's ability to simulate the daily and seasonal cycles of open fires and resulting emissions. Our results indicate that interactive fire emissions are bias low by 32-42%, depending on emitted species, compared to the GFED4s inventory. The bias in emissions drives underestimation in column densities, which is diluted by natural and anthropogenic emissions sources and production and loss mechanisms. Yet, in terms of AOD, a simulation with interactive fire emissions performs just as well as a simulation with prescribed fire emissions.

51

## 52 1 Introduction

Open biomass burning (BB), the outdoor combustion of organic material in the form of vegetation, occurs on every continent, with the exception of Antarctica, at a scale observable from space. Open BB is perceived as a natural ecological process that has been modulating the carbon cycle for more than 420 million years [Scott and Glasspool, 2006]. However, in practice, BB has been mediated by human activities for more than 100,000 years [Bowman et al., 2009, 2011; Archibald et al., 2012]. Bellouin et al. (2008) estimated that at present, only about 20% of fires, compared to preindustrial times, are natural. Andreae (1991) estimated that in the tropics, where about 85% of fire emissions occur [van der Werf et al., 2017], only 10% of fires are natural. In the USA, government records show that about 85% of fires are started by humans [Balch et al., 2017]. Humans



63 affect fires directly through ignition and suppression, and indirectly through man-made  
 64 changes to land surfaces and climate. According to *Hantson et al.* (2015), land-use  
 65 practices are the most important driver of human-fire interactions.

66 BB regimes are often classified based on ecosystem type like boreal, temperate,  
 67 and tropical forests, savanna and grassland, peat land, and agricultural fires [*Ichoku et al.*,  
 68 2012]. However, fire characteristics also vary between geographic regions of the same  
 69 ecosystem type; for example, boreal fires in Russia have very different intensity,  
 70 efficiency, and emissions than boreal fires in Canada [*Wooster and Zhang*, 2004]. *Ichoku*  
 71 *et al.* (2008) suggested an energy-based classification of open BB indicating fire intensity,  
 72 similar to hurricanes, using the radiative power of satellite-retrieved fires. Globally,  
 73 satellite retrievals show that on average about 350 Mha are burned annually [*Giglio et al.*,  
 74 2013; *Chuvieco et al.*, 2016], about 4% of the global vegetated area [*Randerson et al.*,  
 75 2012], an area similar to that of India. African fires contribute about 70% to the global  
 76 total burned area (BA), with about equal contributions from Northern Hemisphere Africa  
 77 (NHAF, Fig. 1) and Southern Hemisphere Africa (SHAF). The most flammable  
 78 ecosystem, globally and specifically in Africa, is the savanna [*Ichoku et al.*, 2008;  
 79 *Randerson et al.*, 2012; *Giglio et al.*, 2013], which in the tropics (23.5° N - 23.5° S) alone  
 80 is responsible for 62% (1341 TgC a<sup>-1</sup>) of global carbon emissions (2200 TgC a<sup>-1</sup>) [*van der*  
 81 *Werf et al.*, 2017]. Australian bushfires (grass and shrub) and South American savanna  
 82 fires are the third and fourth largest regional contributors, with BAs of about 50 Mha and  
 83 20 Mha annually, respectively. Globally, *Randerson et al.* (2012) estimated an additional  
 84 contribution of 120 Mha from small fires. The thermal anomalies used to identify those  
 85 fires, which are mostly associated with agricultural fires, are below the detection limit of  
 86 satellite-retrieved surface reflectance, and come with large uncertainties. Regionally,  
 87 small fires can have a significant contribution to BA. By adding the contribution of small  
 88 fires, burned area increases in Equatorial Asia (EQAS) by 157%, in Central America  
 89 (CEAM) by 143%, and in Southeast Asia (SEAS) by 90% [*Randerson et al.*, 2012]. This  
 90 highlights the regional importance of small agricultural fires to regional fire activity.  
 91 Forest fires, including small fires, contribute about 17 Mha annually to global BA, and  
 92 are dominant in Temperate North America (TENA), Boreal North America (BONA),  
 93 Boreal Asia (BOAS) and EQAS.



94 BB can exist when three conditions are met: fuel is available, fuel is combustible,  
95 and ignition sources are present [Schoennagel *et al.*, 2004]. The coincidence of these  
96 conditions is seasonal, making open BB an inherently seasonal phenomenon. The peak  
97 month and duration of fire season are coupled to the seasonal cycle in precipitation,  
98 especially in the tropics [Giglio *et al.*, 2006; Hantson *et al.*, 2017b]. In North America,  
99 most fires occur over the plains of the Midwest and Southeast from early spring to  
100 summer where they peak in June-July. Those anthropogenic fires are ignited as a mean of  
101 agricultural land clearing. Similarly, around the summer months forest fires are common  
102 along the Rocky Mountains, the Sierra Nevada mountain range, the Pacific Northwest,  
103 and Boreal Canada and Alaska. Forest fires are either ignited on purpose, as part of forest  
104 management practices [Ryan *et al.*, 2013], ignited by accident, as a by-product of the  
105 expansion of urban life to the wildland interface [Moritz *et al.*, 2014; Fischer *et al.*, 2016;  
106 Radeloff *et al.*, 2018], or ignited by lightning [Díaz-Avalos *et al.*, 2001]. In Central  
107 America there is a south-to-north migration of fire activity, which follows the dry season.  
108 Savanna burning in Colombia and Venezuela takes place between January-April,  
109 followed by a May-August burning in Mexico. In South America most of the burning  
110 takes place in the grasslands of southeast Brazil, set by ranchers for land management  
111 practices, from June to mid-October [Dwyer *et al.*, 2000]. In Europe and Eurasia the BB  
112 season is from April to September, with peaks in May, July and August. From April  
113 through August, farmers in the breadbasket of Eurasia, from the Black Sea to Lake Baikal,  
114 start fires to clear the land and burn crop residue. Siberian boreal fires, which are mostly  
115 lightning-ignited, peak in July-August [Dwyer *et al.*, 2000]. Around the same time  
116 Mediterranean fires peak. Trends in population density like land abandonment and shrub  
117 encroachment, fuel the Mediterranean fires [Butsic *et al.*, 2015]. In NHAF the burning  
118 season is from November to March, which peaks in December-January [Giglio *et al.*,  
119 2013]. Then, the shift in the dry season to the Southern hemisphere dictates the SHAF  
120 burning season from May to October, starting in the northwest and progressing to the  
121 southeast [Giglio *et al.*, 2006]. Fires are mostly set on purpose to clear land of crop  
122 residue and parasites, create firebreaks around settlements, and initiate regrowth of  
123 vegetation [Dwyer *et al.*, 2000]. In SEAS the fire season, driven by land management,  
124 starts in January and ends in early April, dictated by the monsoon circulation. BB in





125 eastern Asia, of mainly crop field residue, occurs between May-August. In EQAS  
 126 burning occurs between August and November. In Australia, most fires occur in the  
 127 grasslands of the Northern Territories, starting in the west and progressing to the east  
 128 from May to December. Additionally, fire activity occurs between January and March in  
 129 Southern Australia. The Southern Hemisphere BB activity is particularly sensitive to  
 130 natural modes of variability like El Niño Southern Oscillation (ENSO) [Buchholz *et al.*,  
 131 2018]. During an El Niño year regional BB emissions can be up to two times higher than  
 132 their regional average level, due to increased fire activity in tropical rainforests [van der  
 133 Werf, 2004; Andela and Werf, 2014; Field *et al.*, 2016; Whitburn *et al.*, 2016].

134 Although BB emissions have high spatiotemporal variability, their impact on  
 135 atmospheric composition is significant [Crutzen *et al.*, 1979; Seiler and Crutzen, 1980;  
 136 Crutzen and Andreae, 1990]. BB emissions impact air quality [Johnston *et al.*, 2012,  
 137 2014, 2016; Bauer *et al.*, 2019], and climate [Ward *et al.*, 2012; Lasslop *et al.*, 2019].  
 138 Emitted pollutants include ozone precursors like methane ( $\sim 49 \text{ Tg a}^{-1}$ ), carbon monoxide  
 139 ( $\sim 820 \text{ Tg a}^{-1}$ ), and  $\text{NO}_x$  (mostly emitted as NO,  $\sim 19 \text{ Tg a}^{-1}$ ) [Andreae, 2019]; the latter  
 140 two are also deleterious for health on their own. In addition to gaseous pollutants, BB  
 141 emits particulate matter (a total of  $\sim 85 \text{ Tg a}^{-1}$ ) like primary emitted black carbon ( $\sim 5 \text{ Tg}$   
 142  $\text{a}^{-1}$ ) and organic carbon ( $\sim 36 \text{ Tg a}^{-1}$ ), as well as precursors of brown carbon, and  
 143 secondary organic and inorganic aerosols like non-methane volatile organic compounds  
 144 (NMVOC,  $\sim 58 \text{ Tg a}^{-1}$ ), ammonia ( $\sim 9.9 \text{ Tg a}^{-1}$ ), sulfur dioxide ( $\sim 6 \text{ Tg a}^{-1}$ ), and  $\text{NO}_x$   
 145 [Andreae, 2019]. Exposure to these pollutants at high concentrations or for a long period  
 146 of time can compromise the cardiorespiratory system and lead to death [Lelieveld *et al.*,  
 147 2015]. These pollutants, along with BB-emitted greenhouse gases (GHGs) like carbon  
 148 dioxide ( $\text{CO}_2$ ;  $\sim 13,900 \text{ Tg a}^{-1}$ ) and nitrous oxide ( $\text{N}_2\text{O}$ ;  $\sim 1.38 \text{ Tg a}^{-1}$ ), interact with  
 149 radiation, directly and indirectly. Fires are a net source of carbon dioxide only where  
 150 vegetation regrowth is inhibited, i.e. in deforested areas; otherwise BB is not viewed as a  
 151 source of  $\text{CO}_2$  but as “fast respiration” [van der Werf *et al.*, 2017]. Absorbing black and  
 152 brown carbon [Lack *et al.*, 2012; Lack and Langridge, 2013; Laskin *et al.*, 2015], and  
 153 reflecting primary and secondary organic and inorganic aerosols interact with solar  
 154 radiation directly by scattering and absorbing radiation, and indirectly by modifying  
 155 clouds. The radiative properties of particles and their hygroscopicity are also influenced



156 by their mixing state [Bauer and Menon, 2012]. For example, when black carbon (BC) is  
 157 coated it becomes even more absorbing per unit mass [Bond and Bergstrom, 2006]. There  
 158 is evidence that smoke plumes can suppress or invigorate precipitation [Feingold *et al.*,  
 159 2001; Andreae *et al.*, 2004; Tosca *et al.*, 2015]. Aerosols impact cloud height and cover  
 160 by modifying the heat profile of the atmosphere and increasing the number of cloud  
 161 condensation nuclei. There are large uncertainties associated with aerosols' impact on  
 162 climate. Modeling studies suggest that the aerosol effects from BB emissions overrides  
 163 the BB-GHG effect to a net negative radiative forcing [Mao *et al.*, 2013], with the  
 164 indirect effect of clouds dominating the forcing [Ward *et al.*, 2012]. The present day BB  
 165 forcing is estimated at  $-0.5(-0.1) \pm 0.05 \text{ Wm}^{-2}$  [Ward *et al.*, 2012; Mao *et al.*, 2013; Jiang  
 166 *et al.*, 2016; Landry and Matthews, 2016; Lasslop *et al.*, 2019].

167 The quantification of speciated BB emissions is challenging due to the fact that no  
 168 one fire is the same as another [Ito and Penner, 2005]. The composition of the resulting  
 169 smoke plume depends on the fuel type, burning conditions (i.e. flaming or smoldering),  
 170 fuel consumption, and on background chemistry. More complete combustion has a higher  
 171 fraction of oxidized species (e.g.  $\text{CO}_2$  and  $\text{NO}_x$ ) while smoldering fires release more  
 172 reduced species (e.g. CO,  $\text{NH}_3$ , NMVOCs). Thus, emissions in different regions  
 173 contribute different amounts of pollutants; Indonesia, for example, is responsible for 8%  
 174 of global carbon BB emissions, but 23% of methane BB emissions [van der Werf *et al.*,  
 175 2017]. Emissions are sensitive to season and region. Even within one region, like a boreal  
 176 forest, emissions from crown fires differ from those from ground fires. The amount of  
 177 fuel consumed by a fire is highly variable and depends on fuel load, density, moisture,  
 178 vegetation type, and on environmental factors such as wind speed, soil moisture and soil  
 179 composition. Additional challenges relate to external forcing like insect herbivory,  
 180 mammal grazing, and manmade land fragmentation and deforestation [Schultz *et al.*,  
 181 2008]. The quantification of BB emissions has an even bigger importance during  
 182 preindustrial times, where fire emission are identified as the largest source of uncertainty  
 183 for aerosol loading in Earth system models [Hamilton *et al.*, 2018]. BB emissions are a  
 184 key quantity needed for quantifying the unperturbed-from-humans background conditions  
 185 of the atmosphere [Carslaw *et al.*, 2013].



186 Traditionally, fires are included in climate models using emission inventories  
187 [Lamarque *et al.*, 2010; van der Werf *et al.*, 2010, 2017; van Marle *et al.*, 2017]. Some  
188 models have the ability to simulate BB emissions interactively with a varying level of  
189 complexity [Thonicke *et al.*, 2001; Arora and Boer, 2005; Pechony and Shindell, 2009; Li  
190 *et al.*, 2012; Lasslop *et al.*, 2014; Hantson *et al.*, 2016; Mangeon *et al.*, 2016; Rabin *et al.*,  
191 2017; Zou *et al.*, 2019]. On the one end of the spectrum, there are statistically-based  
192 models, and on the other end there are detailed empirical and physical process-based  
193 models. Statistical models are skilled at making predictions based on present-day  
194 relationships between climate and fire (their training data). Process-based models  
195 encapsulate the complex feedbacks within the climate system at various levels. They  
196 combine physical processes such as fuel condition, cloud-to-ground lightning ignitions,  
197 and wind-driven fire expansion. Some models also include simplified empirical  
198 relationships of anthropogenic ignition and suppression, which, at present, are not  
199 understood in a dynamic process level. Though less accurate than observational datasets,  
200 when trying to simulate individual fire events, fire models provide the unique advantage  
201 of linking the atmosphere, biosphere and hydrosphere in a consistent way, a crucial step  
202 when studying Earth System interactions. They are also able to predict fire during climate  
203 periods for which we have no observational data available (e.g. preindustrial and future).

204 State-of-the-art process-based fire models are well equipped to study the  
205 feedbacks between the climate system and fires [Hantson *et al.*, 2016]. However, there is  
206 indication that they lack accurate predictive capabilities, as they only partly capture  
207 trends in present day observations. For example, satellite products show a global decrease  
208 in burned area from about 500 Mha a<sup>-1</sup> in 1997 to 400 Mha a<sup>-1</sup> in 2013, a trend which fire  
209 models do not capture [Andela *et al.*, 2017]. This trend is mostly driven by land  
210 fragmentation and grazing practices over African savanna, highlighting the challenge of  
211 fire models to account for the combined changes in climate, vegetation and socio-  
212 economic drivers [Forkel *et al.*, 2019].

213 In this paper we present a new global fire module, pyrE, based on an improved  
214 scheme of [Pechony and Shindell, 2009, 2010] with new, state-of-the-art, capabilities.  
215 The pyrE module is process-based, as it includes the two basic parameters of fuel  
216 availability and combustibility, which are used to calculate fire count. It utilizes empirical



relationships with population density to account for the anthropogenic impact on fire ignition and suppression. However, unlike other fire models where fire suppression is applied uniformly across all regions [Rabin *et al.*, 2017], in pyrE fire suppression depends both on population density and region. Additionally, pyrE uses fire count to derive emissions, and is therefore more directly connected to the actual fires, in contrast to other fire models that use BA, a measure more indicative of fire's effect on the landscape. The fire module is part of the NASA GISS ModelE Earth System model, ModelE2.1 (an updated version based on Schmidt *et al.* (2014)), and is described below.

## 2 Model description

pyrE, from the Greek word for fire (pyr), is a global fire module within GISS ModelE. It incorporates the fire count parameterization of Pechony and Shindell (2009, 2010), with the addition of fire spread and BA, following the Community Land Model's (CLM) approach [Li *et al.*, 2012]. The module is a collection of physical processes like flammability, natural and accidental ignition, suppression, fire spread, and fire emissions (Fig. 2). The climate model input required, includes surface temperature, surface relative humidity (RH), precipitation, surface wind speed, vegetation density and type, cloud-to-ground lightning frequency and population density. Like many fire modules it lacks explicit intentional ignition (e.g. crop, deforestation) and peat fires.

### 2.1 Flammability

Flammability is a parameter that indicates conditions favorable for fire occurrence [Pechony and Shindell, 2009, 2010]. It is a unit-less number that ranges between zero and one, and is calculated using vapor pressure deficit (VPD), monthly-accumulated precipitation, and vegetation density (VD).

VPD, an indicator of drought [Seager *et al.*, 2015; Williams *et al.*, 2015], is calculated via the Goff-Gratch equation [Goff and Gratch, 1946; Goff, 1957] using the saturation vapor pressure ( $e_s$ ) and surface relative humidity (RH):

$$VPD = e_s \left( 1 - \frac{RH}{100} \right) \quad (1)$$

Where  $e_{st} = 1013.245$  [mb] is the saturation vapor pressure at the boiling point of water and  $e_s = e_{st} 10^{Z(T)}$  depends on temperature ( $T$ ):

$$Z(T) = a \left( \frac{T_s}{T} - 1 \right) + b \cdot \log \left( \frac{T_s}{T} \right) + c \left( 10^{d \left( 1 - \frac{T_s}{T} \right)} - 1 \right) + f \left( 10^{h \left( \frac{T_s}{T} - 1 \right)} - 1 \right) \quad (2)$$



247 With the coefficients:  $a = -7.90298$ ;  $b = 5.02808$ ;  $c = -1.3816 \cdot 10^{-7}$ ;  $d =$   
 248  $11.344$ ;  $f = 8.1328 \cdot 10^{-3}$ ;  $h = -3.49149$  [Goff and Gratch, 1946], and  $T_s =$   
 249  $373.16$  [°K] (water boiling point temperature).

250 The precipitation dependence of flammability is in the form of an inverse  
 251 exponential (Following [Keetch and Byram, 1968]):

$$252 \quad f(R) = \exp(-c_R R) \quad (3)$$

253 Where  $R$  is the surface rain rate in mm per day and  $c_R = 2$  [day/mm] is an  
 254 empirical constant [Pechony and Shindell, 2009].

255 Vegetation density ( $VD$ ) is taken as the normalized leaf area index (LAI) in the  
 256 land fraction of a grid cell, varying between 0 for no vegetation and 1 for dense  
 257 vegetation.

258 We modified the original calculation proposed by [Pechony and Shindell, 2009]  
 259 by calculating flammability only for the fraction of the model's grid cell that is not  
 260 burned from previous fires. The flammability  $F$  at a time step  $t$  in a grid cell  $(i, j)$  is:

$$261 \quad F(t) = 10^{Z(T(t)_{i,j})} \left(1 - \frac{RH(t)_{i,j}}{100}\right) VD(t)_{i,j} \left(1 - \frac{BA(t)_{i,j}}{LA_{i,j}}\right) \exp(-c_R R(t)_{i,j}) \quad (4)$$

262 Where  $LA_{i,j}$  is the total land area (LA) in the grid cell  $(i, j)$ .

## 263 2.2 Ignition

264 Natural and anthropogenic ignition varies in space and time, and is necessary for  
 265 the calculation of fire count. If ignition is zero, the resulting fire count will be zero,  
 266 independent of flammability. Natural ignition is in the form of cloud-to-ground lightning  
 267 frequency, which is interactively calculated in ModelE2.1 [Price and Rind, 1992, 1993].  
 268 The parameterization of anthropogenic ignition follows Venevsky *et al.* (2002) and is  
 269 based on the assumption that in sparsely populated regions people interact more with the  
 270 natural environment, thus increasing the potential for ignition. The parameterization uses  
 271 population density data and empirical scaling factors, as described by Pechony and  
 272 Shindell (2009), and does not include intentional ignition. The number of anthropogenic  
 273 accidental ignitions per km<sup>2</sup> per month is:

$$274 \quad I_A = k(PD)PD^\alpha \quad (5)$$

275 Where  $PD$  is the population density;  $k(PD) = 6.8PD^{-0.6}$  represents the varying  
 276 anthropogenic ignition potentials as a function of population density;  $\alpha = 0.03$  is the



number of potential ignitions per person per month. Coefficients are taken following *Pechony and Shindell* (2009) and *Mangeon et al.* (2016) which utilized correlation calculations done by *Venevsky et al.* (2002).

### 2.3 Suppression

A first-order approximation of the impact of population density on explicit fire suppression was proposed by *Pechony and Shindell* (2009). According to that parameterization, more fires are suppressed in densely populated areas compared to sparsely populated areas, regardless of ignition source. Specifically, suppression varies from 5% to 95% of fires. However, fire management is a region-specific practice, which depends on cultural norms and economic capabilities. For example, fire suppression in the United States of America (USA) is much more aggressive than most regions in the world. In the Middle East, vegetation is sparse and is mostly near centers of human population for agricultural purposes. Natural ignition is almost inexistent and most fires are controlled by human activities, which make the impact of suppression stronger. Fire suppression for open BB is not commonly practiced in most parts of Africa. In some regions of Africa, fires are used as a tool to clear land for agriculture and to prevent savanna overgrowth and the spread of pests. Hence, we improved the simplistic approach suggested by *Pechony and Shindell* (2009), guided by the results presented in Sect. 5.1.1. We use the complement of the fraction of suppressed fires that is the fraction of non-suppressed fires,  $f_{NS}$ :

$$f_{NS} = \begin{cases} 0.2 \exp(-0.05PD), & \text{USA and MIDE} \\ 1, & \text{Africa} \\ 0.05 + 0.9 \exp(-0.05PD), & \text{Elsewhere} \end{cases} \quad (6)$$

Similarly to *Pechony and Shindell* (2009), constant values are selected in a heuristic manner, due to the lack of appropriate global data.

### 2.4 Fire count

Fire count is a key metric as it is used to drive burned area and fire emissions in pyrE. The number of fires in a time step per  $\text{km}^2$  is calculated as the product of flammability, sum of natural and anthropogenic ignition, and suppression [*Pechony and Shindell*, 2009] (Fig. 2):

$$N_{fire}(t)_{i,j} = F(t)_{i,j} \cdot (I_N(t)_{i,j} + I_A(t)_{i,j}) \cdot f_{NS}(t)_{i,j} \quad (7)$$



## 2.5 Burned area (BA)

We adopted the process-based approach of *Li et al.* (2012) to calculate fire spread and burned area. The burned area in grid cell  $(i, j)$  at a model time step  $t$  is the product of fire count and the weighted average over plant functional types (PFTs) of the area burned by one fire:

$$BA_{i,j} = N_{fire}(t)_{i,j} \cdot \sum_v a_{i,j,v} \cdot f_{i,j,v} \quad (8)$$

Where  $f_{i,j,v}$  is the fractional area covered by plant functional type  $v$ , and the burned area of a single fire  $a_{i,j,v}$  is assumed to have an elliptical shape (Fig. 3). Wind speed, surface relative humidity, and vegetation type control the eccentricity of the ellipsoid that represents the burned area of a single fire (based on *van Wagner* (1969)):

$$a_{i,j,v} = \frac{\pi ROS^2 \tau^3}{4LB} \left(1 + \frac{1}{HB}\right)^2 \quad (9)$$

Where  $ROS$  is the rate of fire spread,  $LB$  is the length-to-breadth ratio, and  $HB$  is the head-to-breadth ratio. The stronger the wind, the more eccentric the ellipse, i.e. the bigger the length-to-breadth ratio:

$$LB = 1 + 10 \cdot (1 - \exp(-0.06W)) \quad (10)$$

Where  $W$  is the surface wind speed in  $\text{m s}^{-1}$ .

Strong winds also increase the head to back ratio; the ratio of the downwind spread compared to the upwind spread:

$$HB = \frac{LB + \sqrt{LB^2 - 1}}{LB - \sqrt{LB^2 - 1}} \quad (11)$$

The rate of spread ( $ROS$ ) of a fire is a function of vegetation type, wind speed, and atmospheric and soil moisture:

$$ROS = ROS_{max} \cdot gW \cdot f_{RH} \cdot f_{\theta} \quad (12)$$

$ROS_{max}$  is the maximum fire spread rate. Following *Li et al.* (2012), we set it to  $0.2 \text{ m s}^{-1}$  for grasses,  $0.17 \text{ m s}^{-1}$  for shrubs,  $0.15 \text{ m s}^{-1}$  for needle leaf trees, and  $0.11 \text{ m s}^{-1}$  for other trees. *Li et al.* (2012) estimated the fire spread coefficients to be on the lower range of observed  $ROS$ , but are yet higher than the global value of  $0.13 \text{ m s}^{-1}$  suggested by *Arora and Boer* (2005).

The limit of the fire spread is set by:

$$gW = \frac{2LB}{1 + \frac{1}{HB}} g_0 \quad (13)$$





335 Where  $g_0 = \frac{1+HB_{max}^{-1}}{2LB_{max}} \approx 0.05$

336  $f_{RH}, f_{\theta}$  are the dependencies of fire spread on RH and root zone soil moisture:

337 
$$f_{RH} = \begin{cases} 1 & RH \leq RH_{low} \\ \frac{RH_{up}-RH}{RH_{up}-RH_{low}} & RH_{low} < RH < RH_{up} \\ 0 & RH \geq RH_{up} \end{cases} \quad (14)$$

338 Following *Li et al.* (2012), we set  $RH_{low} = 30\%$ ,  $RH_{up} = 70\%$  and  $f_{\theta} = 0.5$  as

339 ModelE2.1 does not simulate prognostic root zone soil moisture.

## 340 2.6 Emissions

341 Trace gas and aerosol emissions are calculated using PFT (denoted by  $v$ ) and  
 342 chemical specie ( $s$ ) specific emission factors ( $EF_{s,v}$ ). The emissions per grid cell ( $i, j$ ) of  
 343 specie  $s$  at a model time step  $t$  are calculated by:

344 
$$E_{i,j,s}(t) = N_{fire}(t)_{i,j} \cdot \sum_v EF_{s,v} \cdot f_{i,j,v} \quad (15)$$

345 Where  $E_{i,j,s}(t)$  is the emissions flux rate in  $\text{kg m}^{-2} \text{s}^{-1}$ ,  $N_{fire}(t)_{i,j}$  are the fire  
 346 count,  $EF_{s,v}$  are the offline emission factors, and  $f_v$  is the fractional area of that PFT in  
 347 the grid cell.

348 Emission factors describe the PFT-specific speciated mass (in kg) of the smoke,  
 349 normalized per fire (Table 1). Emission factors were calculated offline using ModelE2.1  
 350 PFTs, annual mean global MODIS Terra fire count, and GFED4s emissions from the  
 351 period of 2003-2009. Our technique, known as multivariate curve fitting, matched the  
 352 emissions within the PFT fraction of the grid cell with the respective fire count. We  
 353 correlated GFED4s emissions with MODIS fire count as a function of the fraction of  
 354 modeled PFTs in a grid cell and calculated different emission factors per PFT.

## 355 2.7 Implementation within ModelE

356 ModelE2.1 can be used with either GFED4s prescribed fire emissions or  
 357 interactive pyrE emissions. The pyrE module generates emissions at every model time  
 358 step with ESM-simulated climate as a driver. Flammability is calculated only in the  
 359 fraction of grid cells with natural vegetation. It is driven by the simulated surface RH,  
 360 surface temperature, monthly accumulated precipitation, and LAI. LAI is calculated by  
 361 Ent [*Kim et al.*, 2015], the Terrestrial Biosphere Model component of ModelE2.1, and is  
 362 currently derived from 2005 MODIS LAI data [*Tian et al.*, 2002a, 2002b]. Cloud-to-





ground lightning, calculated by ModelE2.1, is used as the natural ignition source. Most ESMS have low skill in reproducing flash rate distributions [Murray, 2016], and the GISS model is no exception. A qualitative comparison with the World Wide Lightning Location Network (WWLN) (not presented here) showed that modeled cloud-to-ground lightning, which makes up only about 30% of total lightning, is bias-high in ModelE2.1. We decided to use a simple scaling factor of 0.1 in the calculation of natural ignition to better match observed flash rates, as improving the lightning parameterization is beyond the scope of this study. Gridded population density (PD) that drives both anthropogenic ignition and fire suppression is based on historical data for years prior to 2010 [Klein Goldewijk *et al.*, 2010], and on future projections (not used in this study) for years past 2010. PD has a time resolution of 10 years and is interpolated in between.

The modeling approach presented in this paper provides a good reproduction of the seasonality compared to satellite retrievals (see Results section). However, the simulated magnitude of fire count and burned area was too small compared to satellite retrievals and required the use of a scaling factor, a common practice among other fire models [Pfeifer *et al.*, 2013; Knorr *et al.*, 2014; Hantson *et al.*, 2016; Mangeon *et al.*, 2016; Zou *et al.*, 2019]. To calibrate the global modeled fire count to MODIS retrievals, we used a global scaling factor of 30 for all fire count. A similar approach was taken by Pechony and Shindell (2009). We scaled burned area by a factor of 250 to reach the magnitude of GFED4s. Nevertheless, even with this large correction factor, burned area has a very minor impact on fire count and fire emissions as it accounts for a small fraction of the grid cell that is able to burn.

385

### 386 **3 Model configuration**

We used ModelE2.1 with a spatial resolution of 2° in latitude by 2.5° in longitude, 40 vertical layers and a model top at 0.1 hPa. The vegetation component of ModelE2.1 is the Ent Terrestrial Biosphere Model (Ent TBM), which is coupled with the land use/land cover data in the model [Kim *et al.*, 2015]. Ent prescribes leaf area index (LAI) for 14 plant functional types (presented in Table 1) derived from MODIS 2005 data (cover and biome types [Friedl *et al.*, 2010]; LAI [Tian *et al.*, 2002a, 2002b]), historical crop cover [Pongratz *et al.*, 2008], and vegetation heights from [Simard *et al.*, 2011].



394 In this study we show results from runs of ModelE2.1 coupled to the aerosol  
395 microphysical scheme MATRIX (Multiconfiguration Aerosol TRacker of mIXing state)  
396 [Bauer *et al.*, 2008]. MATRIX simulates aerosol formation, condensation and  
397 coagulation, calculates the size distribution of aerosols and tracks their mixing state. Sea  
398 salt, dust, and dimethyl sulfide (DMS) emissions were calculated interactively, driven by  
399 the simulated climate, while other natural and anthropogenic fluxes, except for fires, were  
400 prescribed from the CEDS (Community Emissions Data System) inventory [Hoesly *et al.*,  
401 2018].

402 In the following, we will present a simulation with pyrE turned on, generating  
403 interactive fire emissions, and a simulation with pyrE turned off, using prescribed 2005  
404 climatological GFED4s emissions instead. Also, we will discuss sensitivity studies using  
405 two simulations where pyrE generates interactive fire emissions but suppression is  
406 changed from a global parameterization to a regional one. Prescribed climatological  
407 monthly varying mean (1996-2004) sea surface temperature and sea ice thickness and  
408 extent were used as boundary conditions [Rayner *et al.*, 2003].

#### 409 **4 Reference datasets**

410 The data below are based on a composite of level 3 Aqua and Terra Moderate-  
411 resolution Imaging Spectro-radiometer (MODIS) Collection 5.1 data [Giglio *et al.*,  
412 2003b; Giglio, 2013], unless otherwise stated. Aqua and Terra are sun-synchronous, near-  
413 polar orbiting satellites with a global continuous record of more than 15 years; Aqua was  
414 launched in May 2002 and Terra in December 1999. Aqua's overpass time is 1:30AM  
415 and 1:30PM local, and Terra's overpass time 10:30AM and 10:30PM local, and their  
416 period is between one to two days. All reference data used in this study are interpolated  
417 and re-gridded to the resolution of ModelE2.1.

#### 418 **4.1 Fire count**

419 To detect fires, MODIS uses brightness temperatures (thermal anomaly) derived  
420 from two channels. Channel 31, that saturates at 400° K, and either channel 21, that  
421 saturates at 500° K, or channel 22, that saturates at 331° K. Channel 22 is preferred over  
422 21 as it has a higher signal to noise ratio, but when it saturates, or has missing data,  
423 channel 21 is used [Justice *et al.*, 2002; Giglio *et al.*, 2006].



424 In our study we used the monthly cloud-corrected fire count (CloudCorrFirePix)  
 425 climate model grid data (MYD14CMH, MOD14CMH). The spatial resolution of the data  
 426 is 0.5°. Static, persistent hot spots are excluded from this product [Giglio, 2013]. Because  
 427 of its non-uniform spatial and temporal sampling, raw MODIS data are biased high at  
 428 high latitudes [Giglio *et al.*, 2003a, 2006]. The product we used is corrected for the  
 429 multiple satellite overpasses, the missing data, and variable cloud cover. Cloud cover  
 430 hinders MODIS retrievals. The fire count in the product we used is normalized to the  
 431 fraction of cloud cover in a pixel. In highly cloudy pixels, the product is set to zero. The  
 432 local time of retrieval matters for fire detection, as fires are driven by the daily cycle in  
 433 solar heating. The largest number of fire count is detected during daytime, with an order  
 434 of magnitude difference between daytime fire count detections and nighttime fire count  
 435 detections [Ichoku *et al.*, 2008]. Thus, differences are evident between the Aqua and  
 436 Terra retrievals. This motivated us to use data from the two satellites in our analysis. We  
 437 calculate and utilize climatological monthly means from the period 2003-2016.

#### 438 **4.2 Burned area**

439 We used burned area from the Global Fire Emissions Database (GFED) version  
 440 4s that includes small fires [van der Werf *et al.*, 2010, 2017; Randerson *et al.*, 2012;  
 441 Giglio *et al.*, 2013]. The GFED4s inventory is based on multi-sensor MODIS data,  
 442 involving both reflectance and thermal anomalies measurements from Aqua and Terra.  
 443 MODIS detects burned area using the 650 nm, 1200 nm, and 2100 nm reflectance bands.  
 444 Retrievals must be free from cloud contamination and free from active fires within the  
 445 500 m MODIS grid cell. First, to generate the GFED4s data, MODIS burned area  
 446 collection 5.1 data (MCD64A1 product) are aggregated to a 0.25° grid. Then, burned area  
 447 from small fires is added. The burned area of small fires is statistically estimated using  
 448 active fire count detected by MODIS (a composite of both Aqua and Terra). Both the  
 449 ratio and correction factor are estimated each year as a function of region, season, and  
 450 vegetation type [Randerson *et al.*, 2012; van der Werf *et al.*, 2017]. Due to the projection  
 451 of the MODIS reflectance product over the thermal anomaly one, some resampling errors  
 452 occur. To partially correct this error, region-specific factors ranging from 0.88 in Africa  
 453 to 1.12 in boreal Asia are applied. In this study we use climatological monthly means of  
 454 burned area from the period 2003-2016.



### 4.3 Biomass burning emission inventory

GFED4s emissions are derived from the multiplication of burned area and fuel consumption [van der Werf *et al.*, 2010, 2017]. As such, they have the same spatial and temporal resolution as burned area, of 0.25° by 0.25° and a month. Fuel consumption is calculated using an estimation of fuel loss and combustion completeness, which are calculated using MODIS-based metrics such as differences in normalized burned area (dNBR), normalized vegetation index (NDVI), and land surface temperature (LST). These metrics inform about changes in green vegetation, canopy and soil water, and landscape charring. The satellite-based data are used as input to the Carnegie–Ames–Stanford Approach (CASA) biogeochemical model [Randerson *et al.*, 1996] to calculate the dry matter burned. Then, emission factors [Andreae and Merlet, 2001; Akagi *et al.*, 2011] are applied to convert the dry matter burned to PFT-specific speciated gas and aerosol phase emissions. Kaiser *et al.* (2012) and Pan *et al.* (2019) showed that there are regional biases in older and current versions of GFED; being especially biased low in the Southern Hemisphere compared to AERONET aerosol optical depth (AOD). In order to eliminate the strong interannual BB variability, our analysis used GFED4s mean climatological data of 1995–2010.

### 4.4 Fire regions

The analysis we present below is based on the widely used fire regions (Fig. 1) as defined by GFED [Giglio *et al.*, 2006; van der Werf *et al.*, 2006]. The regions are defined based on climate and fire regimes, and are widely used as basis regions for global fire studies.

### 4.5 Aerosol optical depth

The impact of fire emissions on atmospheric composition is investigated by comparing monthly Aqua and Terra MODIS retrievals of AOD at 550nm [Remer *et al.*, 2005; Platnick *et al.*, 2015]. AOD describes the entire atmospheric column-integrated extinction of aerosols. MODIS AOD data are a useful tool in the study of simulated BB plumes [Voulgarakis and Field, 2015; Johnson *et al.*, 2016; Bauer *et al.*, 2019]. The AOD data we used has a 1° spatial resolution. The monthly mean data (MYD08\_M3 and MOD08\_M3 products) have been averaged over the period 2003–2007 to create monthly climatologies centered around the year 2005. The AOD product we use includes



improvements made via the Dark Target algorithm [Kaufman *et al.*, 1997], which was developed particularly for retrievals over dark vegetated surfaces [Wei *et al.*, 2019]. However, the algorithm fails at retrieving valid AOD data over bright surfaces like desert areas [Levy *et al.*, 2013], which we discard. Here we use collection 6.1 data.

## 5 Results and discussion

### 5.1 Fire count

#### 5.1.1 Regional suppression

First we want to demonstrate how the parameterization with regionally-dependent fire suppression improves the simulation of fire count compared to the original simplified global fire suppression proposed by Pechony and Shindell (2009) (Fig. 4). Our goal was to improve the fire parameterization in regions where the seasonality was captured in timing but not in magnitude. We propose regional modifications to Africa (NHAF, SHAF), a region that drives global fire activity, and had a distinct mismatch in fire count compared to satellite retrievals. Originally, over NHAF the fire seasonality was too flat, while over SHAF it matched MODIS-Terra, but was orders of magnitude smaller than MODIS-Aqua. Since fire suppression for open BB is not commonly practiced in rural Africa, eliminating it over NHAF and SHAF helped resolve the seasonal cycle (Fig. 4 and Eq. 6). The two other regions we modified are TENA and Middle East (MIDE). Over both of those regions the simulated fire seasonality was too strong. Increasing fire suppression over MIDE and TENA greatly improved our simulations compared to MODIS retrievals.

The pyrE module is skilled at capturing the fire seasonality in regions identified by Forkel *et al.* (2017) as controlled by temperature and wetness (climate controls), like Southern Hemisphere South America (SHSA) (Fig. A1). However, there are regions that our parameterization does not simulate well, mainly due to the fact that the fire activity there is driven by land use practices and intentional fire ignitions, which pyrE does not resolve. For example, in TENA we are missing the spring peak of agricultural fires. Similarly, over Europe and Boreal Asia (Fig. A1) we are missing the winter and spring fires associated with intentional ignition [Dwyer *et al.*, 2000; Ganteaume *et al.*, 2013]. Other regions where the seasonality is not well captured, likely due to the fact that it is driven by intentional ignitions, include Central America, Northern Hemisphere South



America, Central Asia, Southeast Asia, and Equatorial Asia. Over Australia, the model captures neither the magnitude nor the timing of the BB seasonality. This is in part due to the model's poor performance of the simulated cloud-to-ground lightning ignitions in that region (not shown).

In all simulations going forward we used the regional suppression scheme.

### 5.1.2 Daily cycle

We looked at the fire count daily cycle to see if it can explain the differences between Aqua, Terra, and the model. The monthly mean fire count detected by Aqua and Terra is expected to be different due to their different overpass times. In Fig. 5, pyrE simulates a distinct daily cycle in fire count in different locations. The simulated daily cycle is most strongly controlled by the simulated daily cycle in flammability (not presented here), matching the daily solar cycle. pyrE's ability to resolve a daily cycle of fire activity highlights the dynamic nature of a process-based fire model.

Using 30-minute simulation output, we sampled all surface grid cells at the daytime overpass time of MODIS Terra, 10:30am local time, and MODIS Aqua, 1:30pm local time. We focused on the daytime overpass time of Terra and Aqua since about 95% of fire count detections occur then [Ichoku *et al.*, 2008]. Our results in Fig. 6 and Fig. 7 indicate that, globally, simulated fire count sampled at daytime overpass is bias-high compared to MODIS retrievals from the respective satellite, for much of the year. On a global annual mean, the model sampled in daytime Terra overpass time is higher than MODIS Terra fire count by 45%, while the model sampled in daytime Aqua overpass time is higher than MODIS Aqua fire count by 13%. However, this behavior differs by region and maximizes in NH sub-Saharan Africa and SH central Africa. The simulated fire count is bias-low compared to MODIS retrievals along the coast of west Africa, in eastern southeast Asia and Australia. The implications of these findings are that even though the simulated monthly mean fire count is in the range of Terra and Aqua (Fig. 4, A1), the simulated fire count is in fact higher than MODIS retrievals. Considering that the actual number of fire count is likely higher than the number retrieved by MODIS, as cloud contamination is decreasing its detection efficiency, it is conceivable that a model weakly high-biased compare to the satellite retrievals is realistic. All results presented



later were not sampled according to a satellite overpass time, but instead were averaged over the whole length of the day.

## 5.2 Burned area

The simulated burned area is bias-low compared to the GFED4s inventory (Fig. 8, A2). The total annual simulated burned area (10-year climatological mean) is 31.5 Mha while GFED4s burned area (mean of 2003-2016) is 38.1 Mha. However, this behavior is region-specific. The simulated burned area is lower compared to GFED4s over northern hemisphere Africa, particularly in November-December, over central and equatorial Asia, and over Australia. The simulated burned area (Fig. 8, A2) reflects the spatial distribution and seasonality of simulated fire count (Fig. 8, A1). GFED4s burned area and MODIS fire count do not always have the same seasonality, for example during October-December. During this season the satellite-retrieved fires produce a higher burned area relative to other seasons. The fire activity driving this behavior occurs in the savanna of sub-Saharan Africa, and northern hemisphere South America. In those regions and times of the year the normalized mean bias of modeled burned area is at least twice the size of the normalized mean bias of fire count, e.g. in NHAF a bias of 6.5 for burned area and 1-3 for fire count, depending on the MODIS satellite. This implies that for every fire modeled in these regions and season a smaller area is simulated to burn compared to the reference datasets.

Why is the burned area per fire relationship in simulations much weaker than it is in the reference datasets? Two contributing factors are: prescribed PFT and simulated wind. The prescribed PFT distribution present in the model is rudimentary; it is comprised of 11 flammable vegetation types (Table 1). As for surface winds, the simulated wind patterns driving burned area are averaged over a coarse grid cell ( $2^\circ \times 2.5^\circ$ ). Simulated wind does not represent sub-grid scale processes and is not fueled by the fire's energy, which is likely contributing to an underestimation of the spread of burned area. However, though wind directly impacts burned area, it does not play a major role in the distribution of simulated fires, since burned area itself has a minor impact on





fires due to its small percentage in a grid cell. At most burned area reaches less than 18% of the naturally vegetated fraction of a grid cell, and is on average less than 1%.

### 5.3 Emissions

Due to the intricate processes involved in burned area spread, most fire models struggle to reproduce the observed trend [Andela *et al.*, 2017] and seasonality [Hantson *et al.*, 2017a] of burned area. A more direct approach would be to use fire count, similar to the approach of Pechony and Shindell (2009, 2010) and Pechony *et al.* (2013).

The main source regions for fire emissions are NHAf, EQAS, SHSA, and SHAF. Emissions are well simulated over SHSA and SHAF (Fig. A3-A5), both in terms of timing of the seasonality and in magnitude. The main regions where simulated emissions are lower than GFED4s are sub-Saharan Africa and Indonesia (Fig. 8). However, more generally, simulated gaseous and particulate emissions are globally bias low compared to GFED4s emissions (Table 2). This behavior is most prominent in sub-Saharan east Africa and in EQAS, mainly in Indonesia (Fig. 8). To a lesser degree, simulated fire emissions are also weaker compared to GFED4s in the boreal regions (Fig. A3-A5). The contribution from these regions to the global total is an order of magnitude smaller compared to the main source regions.

The weaker emissions compared to GFED4s are responding to the following inputs: offline emissions factors, lack of crop and peat fires, LAI, and prescribed PFTs. The emission factors that generate fire emissions are derived using multivariate statistical analysis. Though we used seven full years (2003-2009) of data to derive the factors, it might have generated biases in emissions. Areas that burn annually are properly sampled, but areas that have a fire cycle that is longer than a seven year might be biased high or low, depending on whether they were included in the training dataset or not. Also, crop and peat fires are not explicitly included in the simulated emissions, as intentional ignition is not parameterized in pyrE. Specifically, fires are not applied to the crop fraction of a grid cell, and peat surfaces are not included in the PFTs. However, our method of deriving the offline emission factors uses MODIS fire count and GFED4s emissions, and does not distinguish between intentional and accidental fires. Hence, intentional fires are indirectly accounted for in the global sum. However, this indirect inclusion of intentional fires does not necessarily add missing fire emissions in the correct locations. The LAI in





Ent, ModeLE's DGVM, is based on 2005 MODIS retrievals. Though we cannot estimate the role that the lack of interactive LAI plays, it is certainly not optimal, neither for fire count simulation, nor for fire emissions that are derived from these fire count. Unlike fire count, fire emissions are strongly tied to the map of PFTs. The offline emission factors are based on prescribed PFTs, and the interactive emissions themselves are applied according to the sub-grid PFT distribution. The prescribed PFT distribution present in the model might be different than reality, and those differences affect emissions. In the model, the PFTs in areas where emissions are bias high compared to GFED4s there is a high percentage (>50%) of the following PFTs: evergreen broadleaf trees (Amazon, central Africa), cold broadleaf trees (northeast America, Europe), and drought broadleaf trees (central Africa and northern India). In EQAS, a region with bias low simulated emissions, close to 100% of the prescribed PFTs is evergreen broadleaf trees, which in reality is replaced by crops. The bias-low emissions in EQAS are very likely tied to the lack of prescribed peat PFT. In areas with bias low emissions modeled PFTs are mainly (>50%) c4 grass (sub-Saharan Africa, Australia), deciduous needle leaf trees (boreal regions), and arid shrubs (S Africa, Australia).

## 5.4 Composition

### 5.4.1 Column load

In order to quantify how the model skill changes with the inclusion of pyrE instead of prescribed emission inventory data in ModeLE2.1, we compare a simulation with interactive fires to a simulation with prescribed BB sources. Though emissions are mostly bias-low compared to GFED4s, this behavior is less evident in the column density (Fig. 9). For most BB emitted species, the simulation with interactive fires has lower column densities than the simulation with prescribed emissions (Table 2) with a bias ranging from -6.3-0.5% for gaseous species, -4.8% for black carbon and -16% for organic aerosol. However, the column densities are only partly driven by fire emissions, as those make up less than 35% of total global emissions of either CO, organic aerosol, and black carbon emissions. Non-emissions production-and-loss mechanisms also impact column densities.

The difference in column densities between the two simulations is greatest over north sub-Saharan Africa, Indonesia, and the boreal regions. The behavior is region-



specific, and some regions like central Africa and northern hemisphere South America have higher column densities compared to the simulation with prescribed emissions. The differences between the two simulations are more prominent for organic aerosol than any of the other species (Fig. 9, Table 2), while the differences in the spatial distribution of CO are marginal.

#### 5.4.2 Aerosol optical depth (AOD)

In Fig. 10 we compare climatologically-simulated clear-sky AOD with MODIS AOD (Aqua) for January, April, July, and October. The conclusions from Terra products are similar to Aqua's, and will not be presented here, for brevity. In a regional perspective, simulated AOD is able to reproduce the seasonality and spatial distribution of MODIS-retrieved pollution over west and central Africa, east and southeast Asia, and the Arabian sea. The simulations of ModelE2.1 has higher AOD compared to MODIS over the tropical eastern Pacific, an artifact due to the model's skill in simulating stratocumulus cloud decks, which have been improved in a newer version of the ESM (ModelE3).

Model performance as a function of interactive versus offline fire emissions is similar in terms of AOD (Fig. 11). Both simulations have persistently lower (0-30%) AODs over central Africa and central South America compared to MODIS. The locations with an outstanding difference in performance between the simulations are in central sub-Saharan Africa in January and July, and over a small area in Indonesia (Kalimantan) during October. In January over central sub-Saharan Africa the simulation with pyrE has AOD values (NHAF regional mean AOD of 0.26) closer to MODIS (NHAF regional mean AOD of 0.2) than a simulation with prescribed fire emissions (NHAF regional mean AOD of 0.33). while in July it is the simulation with pyrE (NHAF regional mean AOD of 0.53) that is more bias high than the prescribed one (NHAF regional mean AOD of 0.46). Over EQAS in October the simulation with prescribed fires has an AOD of ~0.28 while the simulation with pyrE has an AOD of ~0.18. AOD in this region is sensitive to peat fires, which are not included in ModelE, strongly impacting pyrE's results. Globally, mean AOD simulated with interactive fire emissions is 0.142 while mean AOD simulated with prescribed fire emissions is 0.146. The fact that pyrE has a marginal performance in climatological runs when compared against a simulation using



the more accurate offline emissions is a strong indication that it is a robust module that can be used with confidence at time periods where offline emissions are not available.

Finally, we demonstrate the contribution of BB emissions to total clear-sky AOD by comparing the simulations with both prescribed and interactive fire emissions to a simulation that has no fire emissions at all (Fig. 12). In the simulation with prescribed fire emissions, clear sky AOD is on average 10% higher than it is in a simulation with no fire emissions. In a simulation with pyre clear sky AOD is about 7.5% higher than it is in a simulation with no fire emissions. The impact of BB emissions on AOD is most pronounced in the source regions of Africa and the Amazon. In those regions the difference in AOD varies between 0.15-0.3. It is important to note that the differences in AOD are not only due to impact of BB emissions, but also reflect climate variability, which impacts aerosol lifetime and interactive dust emissions.

## 6 Conclusions

The development of pyrE, allowed us for the first time to interactively simulate climate and fire activity with GISS-ModelE2.1. The pyrE module, which is based on the fire parameterizations of *Pechony and Shindell (2009)*, was expanded to include fire spread and burned area, following the approach of *Li et al. (2012)*. This study set out to simulate the climatology of fires, and not individual fire events. Like only a few other fire models [*Zou et al., 2019*], pyrE was developed with consideration of regional behavior. The new fire suppression scheme depends on population density, but also on geographic regions. The new scheme reflects more intense fire suppression in the USA and Middle East, and revokes fire suppression in Africa, which improved the fire count seasonality simulated by pyrE compared to satellite retrievals. Fire count seasonality is well simulated in the fire source regions: the Amazon, SH Africa, and NH Africa, with the exception of being bias-low compared to MODIS during November-December. This is due to the lack in parameterization of intentional ignitions and agricultural fires.

The regional model skill of fire count was also demonstrated in the simulated burned area. Burned area in southern hemisphere Africa was well simulated by the model, while less active fire regions like temperate and boreal North America, Boreal Asia Europe, and Middle were bias high compared to GFED4s. Other regions like Australia, sub-Saharan and West Africa in November-December, Central Asia and Southeast Asia



702 in January-March were bias low. Though the seasonality of simulated burned area  
703 reflects that of simulated fire count, the bias of burned area compared to GFED4s data is  
704 at least double that of fire count. Burned area is a quantity that most fire models struggle  
705 with. Wind speed, a driver of burned area, is averaged over a coarse grid cell, with no  
706 feedback from fire heat and energy, which can be a contributing factor to the lower  
707 simulated burned area values. The prescribed rudimentary PFTs of the model are a  
708 simplified version of the real world and thus can be a source of additional uncertainty.  
709 Finally, the rate of spread of burned area, a function of the burning vegetation type, that  
710 pyrE and other fire models use is on the lower end of field observations. A higher rate of  
711 spread could help to both override the scaling factor used for burned area, and to reduce  
712 the negative bias compared to GFED4s.

713 Unlike other fire models, fire emissions in pyrE are driven directly by fires  
714 instead of burned area. Emissions are based on online fire count calculations and offline  
715 emission factors derived as described in Sect. 2.6. In contrast to the fact that simulated  
716 fire count are bias-high compared to MODIS, globally, fire emissions are bias-low  
717 compared to GFED4s. Fire emissions are well-simulated over the southern hemisphere  
718 with the exception of Australia. Emissions are bias low over the northern hemisphere  
719 including northern sub-Sahara, with the exception of NH South America, which is bias  
720 high. The bias of fire count compared to MODIS in Australia and in sub-Saharan Africa  
721 during November-December propagates to emissions. The emission factors, which were  
722 calculated offline using MODIS fire count and GFED4s fire emissions and were applied  
723 based on the prescribed PFTs of the model, have their own limitations. They are based on  
724 a training dataset of seven years, which would introduce biases in regions where fire  
725 cycle is longer than seven years. Also, they rely on the modeled PFTs, enhancing the  
726 emissions dependency on the prescribed PFT and the lack of peat. Emission factors do  
727 not distinguish between intentional and accidental fires, thus they indirectly account for  
728 all fire emissions, which reduce existing biases, although the regional distribution of them  
729 will not match the locations of intentional fires, unless natural vegetation burning occurs  
730 in the vicinity.

731 Less emissions compared to GFED4s means lower column densities and lower  
732 AOD when comparing a simulation with interactive fires to one with prescribed fires.



733 However, as these quantities depend on climate feedbacks including processes other than  
734 fire, e.g. additional emission sources, precipitation, deposition, transport, and chemistry,  
735 the differences between the two simulations dilute. Nonetheless, a comparison with  
736 MODIS AOD demonstrates that AOD from a simulation with interactive fire emissions is  
737 comparable to AOD from a simulation with prescribed fire emissions.

738 The work presented here highlights that timing matters just as much as magnitude.  
739 This is true for fire distribution, emissions, and atmospheric composition. Timing is also  
740 the reason why intentional ignition was excluded from pyrE. Intentional ignition, namely  
741 land clearing and agricultural fires, depends on region and crop specific planting and  
742 harvesting times. To include it would require crop functionality in ModelE, which was  
743 not present during the time of our development. Further future development should focus  
744 on the inclusion of intentional ignition and agricultural fires which are seasonal in nature,  
745 derived from crop planting and land clearing times. This addition could perhaps improve  
746 model performance over regions like equatorial Asia, Southeast Asia, and Central  
747 America as well as override the global scaling factors applied to fire count and burned  
748 area. The use of scaling factors is a common practice among fire models, and should be  
749 carefully and transparently documented. Also, enhancing the prescribed PFTs, especially  
750 via the addition of peat is imperative when studying fires. Peat exists as well outside of  
751 tropical Asia. There are immense reservoirs of peat in Africa [Dargie *et al.*, 2017], as  
752 well as the boreal regions [Yu, 2012], where it used to be trapped under permafrost. Peat  
753 will likely become an even bigger source of fire emissions in the future. Improvement of  
754 the cloud to ground lightning parameterization may also prove useful, as changes to  
755 natural ignition will likely have significant impacts on Australian and boreal fire  
756 emissions. Finally, almost no fire models include fire energy. However, given that the  
757 heat component of fires interact with the climate system, and can also be used to derive  
758 more accurate emissions (as demonstrated by *Ichoku and Ellison (2014)*), it is worthwhile  
759 taking it into consideration.

760  
761  
762  
763



## 764 7 Code availability

765 pyrE is in line with state-of-the-art fire models, and can be easily applied to other ESMs.  
 766 Information on ModelE, including access to online data and descriptions are available at  
 767 <http://www.giss.nasa.gov/tools/modelE>. The pyrE module is included in ModelE version  
 768 2.1. The source code, along with documentation, can be downloaded from the NASA  
 769 Goddard Institute of Space Studies website: <https://simplex.giss.nasa.gov/snapshots/>.

770 **Acknowledgements.** Climate modeling at GISS is supported by the NASA Modeling,  
 771 Analysis, and Prediction program. The authors acknowledge funding from NASA's  
 772 Atmospheric Composition Modeling and Analysis Program (ACMAP), contract  
 773 NNX15AE36G. Resources supporting this work were provided by the NASA High-End  
 774 Computing (HEC) Program through the NASA Center for Climate Simulation (NCCS) at  
 775 Goddard Space Flight Center.

## 777 References

- 778 Akagi, S. K., R. J. Yokelson, C. Wiedinmyer, M. J. Alvarado, J. S. Reid, T. Karl, J. D.  
 779 Crounse, and P. O. Wennberg: Emission factors for open and domestic biomass  
 780 burning for use in atmospheric models, *Atmos. Chem. Phys.*, *11*(9), 4039–4072,  
 781 doi:10.5194/acp-11-4039-2011, 2011.
- 782 Andela, N., and G. R. Van Der Werf : Recent trends in African fires driven by cropland  
 783 expansion and El Niño to La Niña transition, *4*(September), 791–795,  
 784 doi:10.1038/NCLIMATE2313, 2014.
- 785 Andela, N., D. C. Morton, L. Giglio, Y. Chen, G. R. van der Werf, P. S. Kasibhatla, R. S.  
 786 DeFries, G. J. Collatz, S. Hantson, S. Kloster, D. Bachelet, M. Forrest, G. Lasslop, F.  
 787 Li, S. Mangeon, J. R. Melton, C. Yue, J. T. Randerson: A human-driven decline in  
 788 global burned area, , *1362*(June), 1356–1362, 2017.
- 789 Andreae, M. O.: Biomass burning: Its history, use, and distribution and its impact on  
 790 environmental quality and global climate, in *Global Biomass Burining: Atmosphere,*  
 791 *Climate and Biospheric implications*, edited by J. S. Levine, *MIT Press. Cambridge,*  
 792 *Mass.*, 3–21, 1991.
- 793 Andreae, M. O.: Emission of trace gases and aerosols from biomass burning – An  
 794 updated assessment, *Atmos. Chem. Phys. Discuss.*, *15* (4)(April), 1–27,



- 795        doi:10.5194/acp-2019-303, 2019.
- 796    Andreae, M. O., and P. Merlet: Emission of trace gases and aerosols from biomass  
 797        burning, *Global Biogeochem. Cycles*, *15*(4), 955–966, doi:10.1029/2000GB001382,  
 798        2001.
- 799    Andreae, M. O., D. Rosenfeld, P. Artaxo, A. A. Costa, G. P. Frank, K. M. Longo, and M.  
 800        A. F. Silva-Dias: Smoking rain clouds over the Amazon., *Science*, *303*, 1337–1342,  
 801        doi:10.1126/science.1092779, 2004.
- 802    Archibald, S., A. C. Staver, and S. A. Levin: Evolution of human-driven fire regimes in  
 803        Africa, *Proc. Natl. Acad. Sci.*, *109*(3), 847–852, doi:10.1073/pnas.1118648109,  
 804        2012.
- 805    Arora, V. K., and G. J. Boer: Fire as an interactive component of dynamic vegetation  
 806        models, *J. Geophys. Res.*, *110*, doi:10.1029/2005JG000042, 2005.
- 807    Balch, J. K., B. A. Bradley, J. T. Abatzoglou, R. C. Nagy, and E. J. Fusco: Human-started  
 808        wildfires expand the fire niche across the United States, , *114*(11),  
 809        doi:10.1073/pnas.1617394114, 2017.
- 810    Bauer, S.E., D. Wright, D. Koch, E.R. Lewis, R. McGraw, L.-S. Chang, S.E. Schwartz,  
 811        and R. Ruedy: MATRIX (Multiconfiguration Aerosol TRacker of mIXing state): An  
 812        aerosol microphysical module for global atmospheric models. *Atmos. Chem. Phys.*,  
 813        *8*, 6603–6035, doi:10.5194/acp-8-6003-2008, 2008.
- 814    Bauer, S. E., and S. Menon: Aerosol direct , indirect , semidirect , and surface albedo  
 815        effects from sector contributions based on the IPCC AR5 emissions for preindustrial  
 816        and present-day conditions, , *117*, 1–15, doi:10.1029/2011JD016816, 2012.
- 817    Bauer, S. E., U. Im, K. Mezuman, and C. Y. Gao: Desert dust, industrialization and  
 818        agricultural fires: Health impacts of outdoor air pollution in Africa, *J. Geophys. Res.*  
 819        *Atmos.*, 1–17, doi:10.1029/2018JD029336, 2019.
- 820    Bellouin, N., A. Jones, J. Haywood, and S. A. Christopher: Updated estimate of aerosol  
 821        direct Radiative forcing from satellite observations and comparison against the  
 822        centre climate model, *J. Geophys. Res. Atmos.*, *113*(10), 1–15,  
 823        doi:10.1029/2007JD009385, 2008.
- 824    Bond, T. C., and R. W. Bergstrom: Light Absorption by Carbonaceous Particles: An  
 825        Investigative Review, *Aerosol Sci. Technol.*, *40*(1), 27–67,





- doi:10.1080/02786820500421521, 2006.
- Bowman, D. M. J. S., J. K. Balch, P. Artaxo, W. J. Bond, J. M. Carlson, M. A. Cochrane, C. M. D’Antonio, R. S. DeFries, J. C. Doyle, S. P. Harrison, F. H. Johnston, J. E. Keeley, M. A. Krawchuk, C. A. Kull, J. B. Marston, M. A. Moritz, I. C. Prentice, C. I. Roos, A. C. Scott, T. W. Swetnam, G. R. van der Werf, and S. J. Pyne: Fire in the Earth System, *Science*, 324(5926), 481–484, doi:10.1126/science.1163886, 2009.
- Bowman, D. M. J. S., J. Balch, P. Artaxo, W. J. Bond, M. A. Cochrane, C. M. D’Antonio, R. DeFries, F. H. Johnston, J. E. Keeley, M. A. Krawchuk, C. A. Kull, M. Mack, M. A. Moritz, S. Pyne, C. I. Roos, A. C. Scott, N. S. Sodhi, and T. W. Swetnam: The human dimension of fire regimes on Earth, *J. Biogeogr.*, 38(12), 2223–2236, doi:10.1111/j.1365-2699.2011.02595.x, 2011.
- Buchholz, R. R., D. Hammerling, H. M. Worden, M. N. Deeter, L. K. Emmons, D. P. Edwards, and S. A. Monks: Links Between Carbon Monoxide and Climate Indices for the Southern Hemisphere and Tropical Fire Regions, *J. Geophys. Res. Atmos.*, 123(17), 9786–9800, doi:10.1029/2018JD028438, 2018.
- Butsic, V., M. Kelly, and M. Moritz: Land Use and Wildfire: A Review of Local Interactions and Teleconnections, *Land*, 4(1), 140–156, doi:10.3390/land4010140, 2015.
- Carlsaw, K. S., L. A. Lee, C. L. Reddington, K. J. Pringle, A. Rap, P. M. Forster, G. W. Mann, D. V. Spracklen, M. T. Woodhouse<sup>1</sup>, L. A. Regayre, and J. R. Pierce: Large contribution of natural aerosols to uncertainty in indirect forcing., *Nature*, 503(7474), 67–71, doi:10.1038/nature12674, 2013.
- Chuvieco, E., C. Yue, A. Heil, F. Mouillot, I. Alonso-canas, M. Padilla, J. M. Pereira, D. Oom, and K. Tansey: METHODS A new global burned area product for climate assessment of fire impacts, , 45, 619–629, doi:10.1111/geb.12440, 2016.
- Crutzen, P. J., L. E. Heidt, J. P. Krasnec, W. H. Pollock, and W. Seiler: Biomass burning as a source of atmospheric gases CO, H<sub>2</sub>, N<sub>2</sub>O, NO, CH<sub>3</sub>Cl and COS, *Nature*, 282, 253–256, doi:10.1038/282253a0.
- Crutzen, P. J., and M. O. Andreae (1990), Biomass burning in the tropics: impact on atmospheric chemistry and biogeochemical cycles., *Science*, 250, 1669–1678, doi:10.1126/science.250.4988.1669, 1979.





- 857 Díaz-Avalos, C., D. L. Peterson, E. Alvarado, S. a Ferguson, and J. E. Besag: Space–time  
 858 modelling of lightning-caused ignitions in the Blue Mountains, Oregon, *Can. J. For.*  
 859 *Res.*, *31*, 1579–1593, doi:10.1139/cjfr-31-9-1579, 2001.
- 860 Dwyer, E., S. Pinnock, J. M. Gregoire, and J. M. C. Pereira: Global spatial and temporal  
 861 distribution of vegetation fire as determined from satellite observations, *Int. J.*  
 862 *Remote Sens.*, *21*(6–7), 1289–1302, doi:10.1080/014311600210182, 2000.
- 863 Feingold, G., L. A. Remer, J. Ramaprasad, and Y. J. Kaufman: Analysis of smoke impact  
 864 on clouds in Brazilian biomass burning regions: An extension of Twomey’s  
 865 approach, *J. Geophys. Res.*, *106*(D19), 22907, doi:10.1029/2001JD000732, 2001.
- 866 Field, R. D., G. R. van der Werf, T. Faninc, E. J. Fetzerd, R. Fullerd, H. Jethvae, R.  
 867 Levy, N. J. Liveseyd, M. Luod, O. Torrese, and H. M. Worden: Indonesian fire  
 868 activity and smoke pollution in 2015 show persistent nonlinear sensitivity to El  
 869 Niño-induced drought, *Proc. Natl. Acad. Sci.*, *113*(33), 9204–9209,  
 870 doi:10.1073/pnas.1524888113, 2016.
- 871 Fischer, A. P., T. A. Spies, T. A. Steelman, C. Moseley, B. R. Johnson, J. D. Bailey,  
 872 A. A. Ager, P. Bourgeron, S. Charnley, B. M. Collins, J. D. Kline, J. E. Leahy,  
 873 J. S. Littell, J. D. A. Millington, M. Nielsen-Pincus, C. S. Olsen, T. B. Paveglio, C. I.  
 874 Roos, M. M. Steen-Adams, F. R. Stevens, J. Vukomanovic, E. M. White, and D. M.  
 875 J. S. Bowman: Wildfire risk as a socioecological pathology, *Front. Ecol. Environ.*,  
 876 *14*(5), 276–284, doi:10.1002/fee.1283, 2016.
- 877 Forkel, M., W. Dorigo, G. Lasslop, I. Teubner, E. Chuvieco, and K. Thonicke: A data-  
 878 driven approach to identify controls on global fire activity from satellite and climate  
 879 observations (SOFIA V1), *Geosci. Model Dev.*, *10*(12), 4443–4476,  
 880 doi:10.5194/gmd-10-4443-2017, 2017.
- 881 Forkel, M., N. Andela, S. P. Harrison, G. Lasslop, M. van Marle, E. Chuvieco, W. Dorigo,  
 882 M. Forrest, S. Hantson, A. Heil, F. Li, J. Melton, S. Sitch, C. Yue, and A. Arneth:  
 883 Emergent relationships with respect to burned area in global satellite observations  
 884 and fire-enabled vegetation models, *Biogeosciences*, *16*(1), 57–76, doi:10.5194/bg-  
 885 16-57-2019, 2019.
- 886 Friedl, M. A., D. Sulla-Menashe, B. Tan, A. Schneider, N. Ramankutty, A. Sibley, and X.  
 887 Huang: MODIS Collection 5 global land cover: Algorithm refinements and



- 888 characterization of new datasets, *Remote Sens. Environ.*, *114*, 168–182,  
 889 doi:10.1016/j.rse.2009.08.016, 2010.
- 890 Ganteaume, A., A. Camia, M. Jappiot, J. San-Miguel-Ayanz, M. Long-Fournel, and C.  
 891 Lampin: A review of the main driving factors of forest fire ignition over Europe,  
 892 *Environ. Manage.*, *51*(3), 651–662, doi:10.1007/s00267-012-9961-z, 2013.
- 893 Giglio, L.: MODIS Collection 5 Active Fire Product User’s Guide Version 2.5, *Sci. Syst.*  
 894 *Appl. Inc.*, (March), 61, 2013.
- 895 Giglio, L., J. D. Kendall, and R. Mack: A multi-year active fire dataset for the tropics  
 896 derived from the TRMM VIRS, *Int. J. Remote Sens.*, *24*(22), 4505–4525,  
 897 doi:10.1080/0143116031000070283, 2003a.
- 898 Giglio, L., J. Descloitres, C. O. Justice, and Y. J. Kaufman: An enhanced contextual fire  
 899 detection algorithm for MODIS, *Remote Sens. Environ.*, *87*(2–3), 273–282,  
 900 doi:10.1016/S0034-4257(03)00184-6, 2003b.
- 901 Giglio, L., I. Csiszar, and C. O. Justice: Global distribution and seasonality of active fires  
 902 as observed with the Terra and Aqua Moderate Resolution Imaging  
 903 Spectroradiometer (MODIS) sensors, *J. Geophys. Res. Biogeosciences*, *111*(2), 1–12,  
 904 doi:10.1029/2005JG000142, 2006.
- 905 Giglio, L., J. T. Randerson, and G. R. Van Der Werf: Analysis of daily, monthly, and  
 906 annual burned area using the fourth-generation global fire emissions database  
 907 (GFED4), *J. Geophys. Res. Biogeosciences*, *118*(1), 317–328,  
 908 doi:10.1002/jgrg.20042, 2013.
- 909 Goff, J. A.: Saturation pressure of water on the new Kelvin temperature scale, in  
 910 *Transactions of the American Society of Heating and Ventilating Engineers*, *63rd*  
 911 *Semi-Annual Meeting*, pp. 347–354, Am. Soc. of Heating and Ventilating Eng.,  
 912 Murray Bay, Quebec, Canada, 1957.
- 913 Goff, J. A., and S. Gratch: Low-pressure properties of water from 160 to 212F, in  
 914 *Transactions of the American Society of Heating and Ventilating Engineers*, *52nd*  
 915 *Annual Meeting*, pp. 95–122, Am. Soc. of Heating and Ventilating Eng., New York,  
 916 1946.
- 917 Hamilton, D. S., S. Hantson, C. E. Scott, J. O. Kaplan, K. J. Pringle, L. P. Nieradzick, A.  
 918 Rap, G. A. Folberth, D. V. Spracklen, and K. S. Carslaw: Reassessment of pre-



- 919 industrial fire emissions strongly affects anthropogenic aerosol forcing, *Nat.*  
 920 *Commun.*, 9(1), doi:10.1038/s41467-018-05592-9, 2018.
- 921 Hantson, S., G. Lasslop, S. Kloster, and E. Chuvieco: Anthropogenic effects on global  
 922 mean fire size, *Int. J. Wildl. Fire*, 24(5), 589–596, doi:10.1071/WF14208, 2015.
- 923 Hantson, S., A. Arneth, S. P. Harrison, D. I. Kelley, I. C. Prentice, S. S. Rabin, S.  
 924 Archibald, F. Mouillot, S. R. Arnold, P. Artaxo, D. Bachelet, P. Ciais, M. Forrest, P.  
 925 Friedlingstein, T. Hickler, J. O. Kaplan, S. Kloster, W. Knorr, G. Lasslop, F. Li, S.  
 926 Mangeon, J. R. Melton, A. Meyn, S. Sitch, A. Spessa, G. R. van der Werf, A.  
 927 Voulgarakis, and C. Yue: The status and challenge of global fire modelling,  
 928 *Biogeosciences*, 13(11), 3359–3375, doi:10.5194/bg-13-3359-2016, 2016.
- 929 Hantson, S. et al.: Evaluation of global fire models within the Fire Model  
 930 Intercomparison Project (FireMIP), in *5th iLEAPS Science Conference*, p. E311:  
 931 POSTER-0072, Oxford, UK, 2017a.
- 932 Hantson, S., M. Scheffer, S. Pueyo, C. Xu, G. Lasslop, E. H. Van Nes, M. Holmgren, and  
 933 J. Mendelsohn: Rare, Intense, Big fires dominate the global tropics under drier  
 934 conditions, *Sci. Rep.*, 7(1), 7–11, doi:10.1038/s41598-017-14654-9, 2017b.
- 935 Hoesly, R. M., S. J. Smith, L. Feng, Z. Klimont, G. Janssens-Maenhout, T. Pitkanen, J. J.  
 936 Seibert, L. Vu, R. J. Andres, R. M. Bolt, T. C. Bond, L. Dawidowski, N. Kholod, J.  
 937 Kurokawa, M. Li, L. Liu, Z. Lu, M. C. P. Moura, P. R. O'Rourke, and Q. Zhang:  
 938 Historical (1750–2014) anthropogenic emissions of reactive gases and aerosols from  
 939 the Community Emissions Data System (CEDS), *Geosci. Model Dev.*, 11(1), 369–  
 940 408, doi:10.5194/gmd-11-369-2018, 2018.
- 941 Ichoku, C., L. Giglio, M. J. Wooster, and L. A. Remer: Global characterization of  
 942 biomass-burning patterns using satellite measurements of fire radiative energy,  
 943 *Remote Sens. Environ.*, 112(6), 2950–2962, doi:10.1016/j.rse.2008.02.009, 2008.
- 944 Ichoku, C., and L. Ellison: Global top-down smoke-aerosol emissions estimation using  
 945 satellite fire radiative power measurements, *Atmos. Chem. Phys.*, 14, 6643–6667,  
 946 doi:10.5194/acp-14-6643-2014, 2014.
- 947 Ichoku, C., R. Kahn, and M. Chin: Satellite contributions to the quantitative  
 948 characterization of biomass burning for climate modeling, *Atmos. Res.*, 111, 1–28,  
 949 doi:10.1016/j.atmosres.2012.03.007, 2012.



- 950 Ito, A., and J. E. Penner: Historical emissions of carbonaceous aerosols from biomass and  
 951 fossil fuel burning for the period 1870-2000, *Global Biogeochem. Cycles*, 19(2), 1–  
 952 14, doi:10.1029/2004GB002374, 2005.
- 953 Jiang, Y., Z. Lu, X. Liu, Y. Qian, K. Zhang, Y. Wang, and X.-Q. Yang: Impacts of  
 954 Global Wildfire Aerosols on Direct Radiative, Cloud and Surface-Albedo Forcings  
 955 Simulated with CAM5, *Atmos. Chem. Phys.*, 16, 14805–14824, doi:10.5194/acp-16-  
 956 14805-2016, 2016.
- 957 Johnson, B. T., J. M. Haywood, J. M. Langridge, E. Darbyshire, W. T. Morgan, K. Szpek,  
 958 J. K. Brooke, F. Marengo, H. Coe, P. Artaxo, K. M. Longo, J. P. Mulcahy, G. W.  
 959 Mann, M. Dalvi, and N. Bellouin: Evaluation of biomass burning aerosols in the  
 960 HadGEM3 climate model with observations from the SAMBBA field campaign, ,  
 961 14657–14685, doi:10.5194/acp-16-14657-2016, 2016.
- 962 Johnston, F. H., S. B. Henderson, Y. Chen, J. T. Randerson, M. Marlier, R. S. Defries, P.  
 963 Kinney, D. M. J. S. Bowman, and M. Brauer: Estimated Global Mortality  
 964 Attributable to Smoke from Landscape Fires, , 120(5), 695–701, 2012.
- 965 Johnston, F. H., S. Purdie, B. Jalaludin, K. L. Martin, S. B. Henderson, and G. G. Morgan:  
 966 Air pollution events from forest fires and emergency department attendances in  
 967 Sydney, Australia 1996-2007: A case-crossover analysis, *Environ. Heal. A Glob.*  
 968 *Access Sci. Source*, 13(1), 1–9, doi:10.1186/1476-069X-13-105, 2014.
- 969 Johnston, F. H., S. Melody, and D. M. J. S. Bowman: The pyrohealth transition: How  
 970 combustion emissions have shaped health through human history, *Philos. Trans. R.*  
 971 *Soc. B Biol. Sci.*, 371(1696), doi:10.1098/rstb.2015.0173, 2016.
- 972 Justice, C. ., L. Giglio, S. Korontzi, J. Owens, J. . Morissette, D. Roy, J. Descloitres, S.  
 973 Alleaume, F. Petitcolin, and Y. Kaufman: The MODIS fire products, *Remote Sens.*  
 974 *Environ.*, 83(1–2), 244–262, doi:10.1016/S0034-4257(02)00076-7, 2002.
- 975 Kaiser, J. W., A. Heil, M. O. Andreae, A. Benedetti, N. Chubarova, L. Jones, J.-J.  
 976 Morcrette, M. Razinger, M. G. Schultz, M. Suttie, and G. R. van der Werf: Biomass  
 977 burning emissions estimated with a global fire assimilation system based on  
 978 observed fire radiative power, *Biogeosciences*, 9(1), 527–554, doi:10.5194/bg-9-  
 979 527-2012, 2012.
- 980 Kaufman, Y. J., A. E. Wald, L. A. Remer, B. C. Gao, R. R. Li, and L. Flynn: MODIS



- 981 2.1- $\mu\text{m}$  channel - correlation with visible reflectance for use in remote sensing of  
 982 aerosol, *IEEE Trans. Geosci. Remote Sens.*, 35(5), 1286–1298,  
 983 doi:10.1109/36.628795, 1997.
- 984 Keetch, J. J. J., and G. M. G. M. Byram: A drought index for forest fire control, *Notes*,  
 985 *E-38. Ashe*, 35, doi:10.1016/j.accpm.2015.04.007, 1968.
- 986 Kim, Y., P. R. Moorcroft, I. Aleinov, M. J. Puma, and N. Y. Kiang: Variability of  
 987 phenology and fluxes of water and carbon with observed and simulated soil moisture  
 988 in the Ent Terrestrial Biosphere Model (Ent TBM version 1.0.1.0.0), *Geosci. Model*  
 989 *Dev.*, 8(12), 3837–3865, doi:10.5194/gmd-8-3837-2015, 2015.
- 990 Klein Goldewijk, K., a. Beusen, and P. Janssen: Long-term dynamic modeling of global  
 991 population and built-up area in a spatially explicit way: HYDE 3.1, *The Holocene*,  
 992 20(4), 565–573, doi:10.1177/0959683609356587, 2010.
- 993 Knorr, W., T. Kaminski, A. Arneth, and U. Weber: Impact of human population density  
 994 on fire frequency at the global scale, *Biogeosciences*, 11(4), 1085–1102,  
 995 doi:10.5194/bg-11-1085-2014, 2014.
- 996 Lack, D. A., J. M. Langridge, R. Bahreini, C. D. Cappa, and A. M. Middlebrook: Brown  
 997 carbon and internal mixing in biomass burning particles, , 109(37),  
 998 doi:10.1073/pnas.1206575109/-  
 999 /DCSupplemental.www.pnas.org/cgi/doi/10.1073/pnas.1206575109, 2012.
- 1000 Lack, D. a., and J. M. Langridge: On the attribution of black and brown carbon light  
 1001 absorption using the Ångström exponent, *Atmos. Chem. Phys.*, 13(20), 10535–10543,  
 1002 doi:10.5194/acp-13-10535-2013, 2013.
- 1003 Lamarque, J. F., T. C. Bond, V. Eyring, C. Granier, A. Heil, Z. Klimont, D. Lee, C.  
 1004 Liousse, A. Mieville, B. Owen, M. G. Schultz, D. Shindell, S. J. Smith, E. Stehfest, J.  
 1005 Van Aardenne, O. R. Cooper, M. Kainuma, N. Mahowald, J. R. McConnell, V. Naik,  
 1006 K. Riahi, and D. P. van Vuuren: Historical (1850–2000) gridded anthropogenic and  
 1007 biomass burning emissions of reactive gases and aerosols: methodology and  
 1008 application, *Atmos. Chem. Phys.*, 10(15), 7017–7039, doi:10.5194/acp-10-7017-  
 1009 2010, 2010.
- 1010 Landry, J.-S., and H. D. Matthews: Non-deforestation fire vs. fossil fuel combustion: the  
 1011 source of CO<sub>2</sub> emissions affects the global carbon cycle and climate responses,



- 1012 *Biogeosciences*, 13(7), 2137–2149, doi:10.5194/bg-13-2137-2016, 2016.
- 1013 Laskin, A., J. Laskin, and S. A. Nizkorodov: Chemistry of Atmospheric Brown Carbon,
- 1014 *Chem. Rev.*, 115(10), 4335–4382, doi:10.1021/cr5006167, 2015.
- 1015 Lasslop, G., K. Thonicke, and S. Kloster: SPITFIRE within the MPI Earth system model:
- 1016 Model development and evaluation, *J. Adv. Model. Earth Syst.*, 6, 740–755,
- 1017 doi:10.1002/2013MS000284.Received, 2014.
- 1018 Lasslop, G., A. I. Coppola, A. Voulgarakis, C. Yue, and S. Veraverbeke: Influence of
- 1019 Fire on the Carbon Cycle and Climate, *Curr. Clim. Chang. Reports*,
- 1020 doi:10.1007/s40641-019-00128-9, 2019.
- 1021 Lelieveld, J., J. S. Evans, M. Fnais, D. Giannadaki, and A. Pozzer: The contribution of
- 1022 outdoor air pollution sources to premature mortality on a global scale., *Nature*,
- 1023 525(7569), 367–71, doi:10.1038/nature15371, 2015.
- 1024 Levy, R. C., S. Mattoo, L. A. Munchak, L. A. Remer, A. M. Sayer, F. Patadia, and N. C.
- 1025 Hsu: The Collection 6 MODIS aerosol products over land and ocean, *Atmos. Meas.*
- 1026 *Tech.*, 6(11), 2989–3034, doi:10.5194/amt-6-2989-2013, 2013.
- 1027 Li, F., X. D. Zeng, and S. Levis: A process-based fire parameterization of intermediate
- 1028 complexity in a dynamic global vegetation model, *Biogeosciences*, 9(7), 2761–2780,
- 1029 doi:10.5194/bg-9-2761-2012, 2012.
- 1030 Mangeon, S., A. Voulgarakis, R. Gilham, A. Harper, S. Sitch, and G. Folberth:
- 1031 INFERNO : a fire and emissions scheme for the UK Met Office’s Unified Model,
- 1032 2685–2700, doi:10.5194/gmd-9-2685-2016, 2016.
- 1033 Mao, J., L. W. Horowitz, V. Naik, S. Fan, J. Liu, and A. M. Fiore: Sensitivity of
- 1034 tropospheric oxidants to biomass burning emissions: Implications for radiative
- 1035 forcing, *Geophys. Res. Lett.*, 40(2), 1241–1246, doi:10.1002/grl.50210, 2013.
- 1036 Van Marle, M.J.E., S. Kloster, B.I. Magi, J.R. Marlon, A.-L. Daniau, R.D. Field, A.
- 1037 Arneth, M. Forrest, S. Hantson, N.M. Kehrwald, W. Knorr, G. Lasslop, F. Li, S.
- 1038 Mangeon, C. Yue, J.W. Kaiser, and G.R. van der Werf: Historic global biomass
- 1039 burning emissions for CMIP6 (BB4CMIP) based on merging satellite observations
- 1040 with proxies and fire models (1750-2015). *Geosci. Model Dev.*, 10, 3329-3357,
- 1041 doi:10.5194/gmd-10-3329-2017, 2017.
- 1042 Moritz, M. A., E. Batllori, R. A. Bradstock, A. M. Gill, J. Handmer, P. F. Hessburg, J.



- 1043 Leonard, S. McCaffrey, D. C. Odion, T. Schoennagel, and A. D. Syphard: Learning  
 1044 to coexist with wildfire, *Nature*, 515(7525), 58–66, doi:10.1038/nature13946, 2014.
- 1045 Murray, L. T.: Lightning NO<sub>x</sub> and Impacts on Air Quality, *Curr. Pollut. Reports*, (x),  
 1046 doi:10.1007/s40726-016-0031-7, 2016.
- 1047 Pan, X., Ichoku, C., Chin, M., Bian, H., Darmenov, A., Colarco, P., Ellison, L., Kucsera,  
 1048 T., da Silva, A., Wang, J., Oda, T., and Cui, G.: *Six Global Biomass Burning*  
 1049 *Emission Datasets: Inter-comparison and Application in one Global Aerosol Model*,  
 1050 *Atmos. Chem. Phys. Discuss.*, <https://doi.org/10.5194/acp-2019-475>, in review,  
 1051 2019.
- 1052 Pechony, O., and D. T. Shindell: Fire parameterization on a global scale, *J. Geophys. Res.*  
 1053 *Atmos.*, 114, doi:10.1029/2009JD011927, 2009.
- 1054 Pechony, O., and D. T. Shindell: Driving forces of global wildfires over the past  
 1055 millennium and the forthcoming century, *Proc. Natl. Acad. Sci.*, 107(45), 19167–  
 1056 19170, doi:10.1073/pnas.1003669107, 2010.
- 1057 Pechony, O., D. T. Shindell, and G. Faluvegi: Direct top-down estimates of biomass  
 1058 burning CO emissions using TES and MOPITT versus bottom-up GFED inventory,  
 1059 *J. Geophys. Res. Atmos.*, 118, 8054–8066, doi:10.1002/jgrd.50624, 2013.
- 1060 Pfeifer, E. M., a. Spessa, and J. O. Kaplan: A model for global biomass burning in  
 1061 preindustrial time: LPJ-LMfire (v1.0), *Geosci. Model Dev.*, 6, 643–685,  
 1062 doi:10.5194/gmd-6-643-2013, 2013.
- 1063 Platnick, S., M. D. King, K. G. Meyer, G. Wind, N. Amarasinghe, B. Marchant, G. T.  
 1064 Aronold, Z. ZHANG, P. A. Hubanks, B. Ridgway, J. Riedi: MODIS Cloud Optical  
 1065 Properties: User Guide for the Collection 6/6.1 Level-2 MOD06/MYD06 Product  
 1066 and Associated Level-3 Datasets,  
 1067 doi:[https://doi.org/10.5067/MODIS/MOD08\\_M3.006](https://doi.org/10.5067/MODIS/MOD08_M3.006), 2015.
- 1068 Pongratz, J., C. Reick, T. Raddatz, and M. Claussen: A reconstruction of global  
 1069 agricultural areas and land cover for the last millennium, *Global Biogeochem.*  
 1070 *Cycles*, 22, doi:10.1029/2007GB003153, 2008.
- 1071 Price, C., and D. Rind: A Simple Lightning Parameterization for Calculating Global  
 1072 Lightning Distributions, *J. Geophys. Res.*, 97(D9), 9919–9933, 1992.
- 1073 Price, C., and D. Rind: What Determines The Cloud-to-Ground Lightning Fraction,





- 1074 *Geophys. Res. Lett.*, 20(6), 463–466, 1993.
- 1075 Rabin, S. S., J. R. Melton, G. Lasslop, D. Bachelet, M. Forrest, and S. Hantson: The Fire  
 1076 Modeling Intercomparison Project ( FireMIP ), phase 1 : experimental and analytical  
 1077 protocols with detailed model descriptions, , 1175–1197, doi:10.5194/gmd-10-1175-  
 1078 2017, 2017.
- 1079 Radeloff, V. C., David P. H., H. A. Kramera, M. H. Mockrinb, P. M. Alexandria, A. Bar-  
 1080 Massadac, V. Butsicd, T. J. Hawbakere, S. Martinuzzia, A. D. Syphardf, and S. I.  
 1081 Stewart: Rapid growth of the US wildland-urban interface raises wildfire risk, *Proc.*  
 1082 *Natl. Acad. Sci.*, 201718850, doi:10.1073/pnas.1718850115, 2018.
- 1083 Randerson, J. T., M. V. Thompson, C. M. Malmstrom, C. B. Field, and I. Y. Fung:  
 1084 Substrate limitations for heterotrophs: Implications for models that estimate the  
 1085 seasonal cycle of atmospheric CO<sub>2</sub>, *Global Biogeochem. Cycles*, 10(4), 585–602,  
 1086 doi:10.1029/96GB01981, 1996.
- 1087 Randerson, J. T., Y. Chen, G. R. Van Der Werf, B. M. Rogers, and D. C. Morton: Global  
 1088 burned area and biomass burning emissions from small fires, *J. Geophys. Res.*  
 1089 *Biogeosciences*, 117(4), doi:10.1029/2012JG002128, 2012.
- 1090 Rayner, N. A., D. E. Parker, E. B. Horton, C. K. Folland, L. V. Alexander, D. P. Rowell,  
 1091 E. C. Kent, and A. Kaplan: Global analyses of sea surface temperature, sea ice, and  
 1092 night marine air temperature since the late nineteenth century, *J. Geophys. Res.*,  
 1093 108(D14), 4407, doi:10.1029/2002JD002670, 2003.
- 1094 Remer, L. A., Y. J. Kaufman, D. Tanré , S. Mattoo, D. A. Chu, J. V. Martins,  
 1095 R.-R. Li, C. Ichoku, R. C. Levy, R. G. Kleidman, T. F. Eck, E. Vermote, and B. N.  
 1096 Holben: The MODIS Aerosol Algorithm, Products, and Validation, *J. Atmos. Sci.*,  
 1097 62(4), 947–973, doi:10.1175/JAS3385.1, 2005.
- 1098 Ryan, K. C., E. E. Knapp, and J. M. Varner: Prescribed fire in North American forests  
 1099 and woodlands: History, current practice, and challenges, *Front. Ecol. Environ.*,  
 1100 11(SUPPL. 1), doi:10.1890/120329, 2013.
- 1101 Schmidt, G.A., M. Kelley, L. Nazarenko, R. Ruedy, G.L. Russell, I. Aleinov, M. Bauer,  
 1102 S.E. Bauer, M.K. Bhat, R. Bleck, V. Canuto, Y.-H. Chen, Y. Cheng, T.L. Clune, A.  
 1103 Del Genio, R. de Fainchtein, G. Faluvegi, J.E. Hansen, R.J. Healy, N.Y. Kiang, D.  
 1104 Koch, A.A. Lacis, A.N. LeGrande, J. Lerner, K.K. Lo, E.E. Matthews, S. Menon,





- 1105 R.L. Miller, V. Oinas, A.O. Oloso, J.P. Perlwitz, M.J. Puma, W.M. Putman, D. Rind,  
 1106 A. Romanou, M. Sato, D.T. Shindell, S. Sun, R.A. Syed, N. Tausnev, K. Tsigaridis,  
 1107 N. Unger, A. Voulgarakis, M.-S. Yao, and J. Zhang: Configuration and assessment  
 1108 of the GISS ModelE2 contributions to the CMIP5 archive. *J. Adv. Model. Earth*  
 1109 *Syst.*, 6, no. 1, 141–184, doi:10.1002/2013MS000265, 2014.
- 1110 Schoennagel, T., T. T. Veblen, and W. H. Romme: The Interaction of Fire, Fuels, and  
 1111 Climate across Rocky Mountain Forests, *Bioscience*, 54(JULY), 393–402,  
 1112 doi:10.1641/0006-3568(2004)054, 2004.
- 1113 Schultz, M. G., A. Heil, J. J. Hoelzemann, A. Spessa, K. Thonicke, J. G. Goldammer, A.  
 1114 C. Held, J. M. C. Pereira, and M. van het Bolscher: Global wildland fire emissions  
 1115 from 1960 to 2000, *Global Biogeochem. Cycles*, 22(2), doi:10.1029/2007GB003031,  
 1116 2008.
- 1117 Scott, A. C., and I. J. Glasspool: The diversification of Paleozoic fire systems and  
 1118 fluctuations in atmospheric oxygen concentration, *Proc. Natl. Acad. Sci.*, 103(29),  
 1119 10861–10865, doi:10.1073/pnas.0604090103, 2006.
- 1120 Seager, R., A. Hooks, A. P. Williams, B. Cook, J. Nakamura, and N. Henderson:  
 1121 Climatology, variability, and trends in the U.S. Vapor pressure deficit, an important  
 1122 fire-related meteorological quantity, *J. Appl. Meteorol. Climatol.*, 54(6), 1121–1141,  
 1123 doi:10.1175/JAMC-D-14-0321.1, 2015.
- 1124 Seiler, W., and P. J. Crutzen: Estimates of gross and net fluxes of carbon between the  
 1125 biosphere and the atmosphere from biomass burning, *Clim. Change*, 2, 207–247,  
 1126 doi:10.1007/BF00137988, 1980.
- 1127 Simard, M., N. Pinto, J. B. Fisher, and A. Baccini: Mapping forest canopy height globally  
 1128 with spaceborne lidar, *J. Geophys. Res. Biogeosciences*, 116, 1–12,  
 1129 doi:10.1029/2011JG001708, 2011.
- 1130 Thonicke, K., S. Venevsky, S. Sitch, and W. Cramer: The role of fire disturbance for  
 1131 global vegetation dynamics: coupling fire into a Dynamic Global Vegetation Model,  
 1132 *Glob. Ecol. Biogeogr.*, 10, 661–677, doi:10.1046/j.1466-822X.2001.00175.x, 2001.
- 1133 Tian, Y., C. E. Woodcock, Y. Wang, J. L. Privette, N. V. Shabanov, L. Zhou, Y. Zhang,  
 1134 W. Buermann, J. Dong, B. Veikkanen, Tuomas Häme, K. Andersson, M. Ozdogan,  
 1135 Y. Knyazikhin, R. B. Myneni: Multiscale analysis and validation of the MODIS LAI



- 1136 product I. Uncertainty assessment, *Remote Sens. Environ.*, **83**, 414–430,  
 1137 doi:10.1016/S0034-4257(02)00047-0, 2002a.
- 1138 Tian, Y., C. E. Woodcock, Y. Wang, J. L. Privette, N. V. Shabanov, L. Zhou, Y. Zhang,  
 1139 W. Buermann, J. Dong, B. Veikkanen, Tuomas Häme, K. Andersson, M. Ozdogan,  
 1140 Y. Knyazikhin, R. B. Myneni: Multiscale analysis and validation of the MODIS LAI  
 1141 product II. Sampling strategy, *Remote Sens. Environ.*, **83**, 431–441,  
 1142 doi:10.1016/S0034-4257(02)00058-5, 2002b.
- 1143 Tosca, M. G., D. J. Diner, M. J. Garay, and O. V. Kalashnikova: Human-caused fires  
 1144 limit convection in tropical Africa: First temporal observations and attribution,  
 1145 *Geophys. Res. Lett.*, **42**(15), 6492–6501, doi:10.1002/2015GL065063, 2015.
- 1146 Venevsky, S., K. Thonicke, S. Sitch, and W. Cramer: Simulating fire regimes in human-  
 1147 dominated ecosystems: Iberian Peninsula case study, *Glob. Chang. Biol.*, **8**, 984–998,  
 1148 doi:10.1046/j.1365-2486.2002.00528.x, 2002.
- 1149 Voulgarakis, A., and R. D. Field: Fire Influences on Atmospheric Composition, Air  
 1150 Quality and Climate, *Curr. Pollut. Reports*, **1**(2), 70–81, doi:10.1007/s40726-015-  
 1151 0007-z, 2015.
- 1152 van Wagner, C. E.: A simple fire-growth model, *For. Chron.*, **45**(2), 103–104,  
 1153 doi:10.5558/tfc45104-2, 1969.
- 1154 Ward, D. S., S. Kloster, N. M. Mahowald, B. M. Rogers, J. T. Randerson, and P. G. Hess:  
 1155 The changing radiative forcing of fires: global model estimates for past, present and  
 1156 future, *Atmos. Chem. Phys.*, **12**(22), 10857–10886, doi:10.5194/acp-12-10857-2012,  
 1157 2012.
- 1158 Wei, J., Z. Li, Y. Peng, and L. Sun: MODIS Collection 6.1 aerosol optical depth products  
 1159 over land and ocean: validation and comparison, *Atmos. Environ.*, **201**(October  
 1160 2018), 428–440, doi:10.1016/j.atmosenv.2018.12.004, 2019.
- 1161 van der Werf, G. R.: Continental-Scale Partitioning of Fire Emissions During the 1997 to  
 1162 2001 El Nino/La Nina Period, *Science*, **303**(5654), 73–76,  
 1163 doi:10.1126/science.1090753, 2004.
- 1164 van der Werf, G. R., J. T. Randerson, L. Giglio, G. J. Collatz, P. S. Kasibhatla, and a. F.  
 1165 Arellano: Interannual variability of global biomass burning emissions from 1997 to  
 1166 2004, *Atmos. Chem. Phys.*, **6**, 3423–3441, https://doi.org/10.5194/acp-6-3423-2006,



- 1167 2006.
- 1168 van der Werf, G. R., J. T. Randerson, L. Giglio, G. J. Collatz, M. Mu, P. S. Kasibhatla, D.  
 1169 C. Morton, R. S. DeFries, Y. Jin, and T. T. van Leeuwen: Global fire emissions and  
 1170 the contribution of deforestation, savanna, forest, agricultural, and peat fires (1997–  
 1171 2009), *Atmos. Chem. Phys.*, *10*(23), 11707–11735, doi:10.5194/acp-10-11707-2010,  
 1172 2010.
- 1173 van der Werf, G. R., J. T. Randerson, L. Giglio, T. T. van Leeuwen, Y. Chen, B. M.  
 1174 Rogers, M. Mu, M. J. E. van Marle, D. C. Morton, G. J. Collatz, R. J. Yokelson, and  
 1175 P. S. Kasibhatla: Global fire emissions estimates during 1997–2016, *Earth Syst. Sci.*  
 1176 *Data*, *9*(2), 697–720, doi:10.5194/essd-9-697-2017, 2017.
- 1177 Whitburn, S., M. Van Damme, L. Clarisse, S. Turquety, C. Clerbaux, and P. Coheur:  
 1178 Doubling of annual ammonia emissions from the peat fires in Indonesia during the  
 1179 2015 El Niño, , doi:10.1002/2016GL070620.Received, 2016.
- 1180 Williams, A. P., R. Seager, A. K. Macalady, M. Berkelhammer, M. A. Crimmins, T. W.  
 1181 Swetnam, A. T. Trugman, N. Buening, D. Noone, N. G. McDowell, N. Hryniw, C.  
 1182 I. Mora, and T. Rahn: Correlations between components of the water balance and  
 1183 burned area reveal new insights for predicting forest fire area in the southwest  
 1184 United States, *Int. J. Wildl. Fire*, *24*(1), 14, doi:10.1071/WF14023, 2015.
- 1185 Wooster, M. J., and Y. H. Zhang: Boreal forest fires burn less intensely in Russia than in  
 1186 North America, *Geophys. Res. Lett.*, *31*(20), 2–4, doi:10.1029/2004GL020805, 2004.
- 1187 Zou, Y., Y. Wang, Z. Ke, H. Tian, J. Yang, and Y. Liu: Development of a REgion-  
 1188 Specific Ecosystem Feedback Fire (RESFire) Model in the Community Earth  
 1189 System Model, *J. Adv. Model. Earth Syst.*, *11*(2), 417–445,  
 1190 doi:10.1029/2018MS001368, 2019.
- 1191
- 1192
- 1193
- 1194
- 1195
- 1196
- 1197



# 1198 **Tables**

1199 Table 1 Fire emission factors for the different plant functional types (PFTs) in ModelE2.1.  
 1200 Factors are in units of kg per fire per PFT in the grid cell. For organic and black carbon  
 1201 units kg is substituted with kg of carbon.

PFT	CO	NO <sub>x</sub>	SO <sub>2</sub>	NH <sub>3</sub>	Alkenes	Paraffin	OC	BC
Cold Broadleaf	113392	1529	555	2101	106	69.8	3437	767
Deciduous	481485	1559	4168	10722	422	373	36753	1844
Needle leaf								
Drought	230829	4835	1687	2340	214	108	10667	1382
Broadleaf								
Evergreen	249906	4905	1438	2847	220	102	10941	1434
Broadleaf								
Evergreen	146622	1197	972	2277	137	89.1	6537	821
Needle leaf								
Cold Shrub	105936	241	878	2006	104	72.1	6562	357
Arid Shrub	39268	1009	262	378	36.6	18.5	1479	238
C3 Annual	26761	690	147	313	25.1	13.9	728	173
Grass								
C3 Arctic	251702	1094	2315	5065	489	226	15551	1159
Grass								
C3 Perennial	41043	908	270	438	38.8	20.7	1504	257
Grass								
C4 Grass	117577	3152	795	1196	110	57	4339	726

1202  
 1203  
 1204  
 1205  
 1206  
 1207  
 1208  
 1209



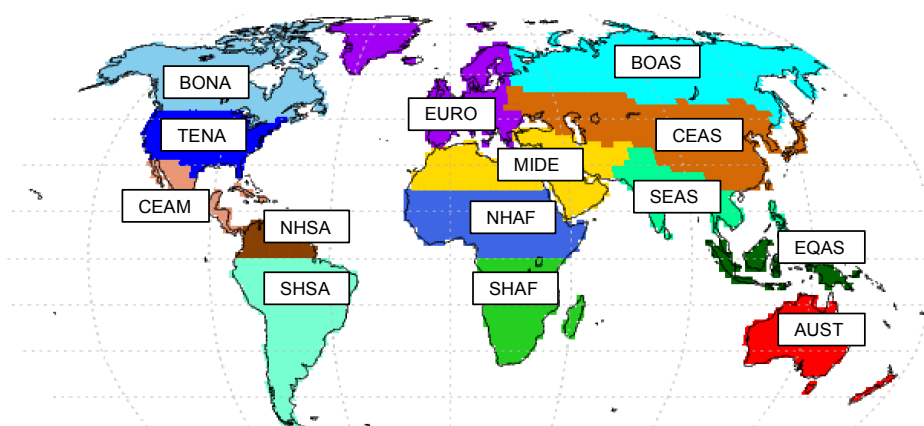
Table 2: Total fire emissions and global mean column loads of fire emitted species.

Species	Variable	pyrE	GFED4s	Bias [%]
CO	Emissions [Tg a <sup>-1</sup> ]	2.14E+02	3.51E+02	-39
	Column Load [kg m <sup>-2</sup> ]	7.22E-04	7.71E-04	-6.3
OA	Emissions [TgC a <sup>-1</sup> ]	1.31E+01	2.29E+01	-42
	Column Load [kg m <sup>-2</sup> ]	8.52E-07	1.02E-06	-16
BC	Emissions [TgC a <sup>-1</sup> ]	1.25E+00	1.84E+00	-32
	Column Load [kg m <sup>-2</sup> ]	7.25E-09	7.62E-09	-4.8
NO <sub>x</sub>	Emissions [Tg a <sup>-1</sup> ]	4.27E+00	6.76E+00	-36
	Column Load [kg m <sup>-2</sup> ]	5.94E-07	5.91E-07	0.5
NH <sub>3</sub>	Emissions [Tg a <sup>-1</sup> ]	2.43E+00	4.15E+00	-41
	Column Load [kg m <sup>-2</sup> ]	2.15E-07	2.23E-07	-3.5
SO <sub>2</sub>	Emissions [Tg a <sup>-1</sup> ]	1.34E+00	2.25E+00	-40
	Column Load [kg m <sup>-2</sup> ]	2.67E-06	2.69E-06	-0.7
Alkenes	Emissions [Tg a <sup>-1</sup> ]	1.94E-01	3.18E-01	-39
	Column Load [kg m <sup>-2</sup> ]	5.73E-08	5.70E-08	0.5
Paraffin	Emissions [Tg a <sup>-1</sup> ]	9.79E-02	1.65E-01	-40
	Column Load [kg m <sup>-2</sup> ]	2.36E-07	2.42E-07	-2.4



1223

## 1224 FIGURES



1225

BONA Boreal North America	NHAf Northern Hemisphere Africa
TENA Temperate North America	SHAF Southern Hemisphere Africa
CEAM Central America	BOAS Boreal Asia
NHSA Northern Hemisphere South America	CEAS Central Asia
SHSA Southern Hemisphere South America	SEAS Southeast Asia
EURO Europe	EQAS Equatorial Asia
MIDE Middle East	AUST Australia and New Zealand

1226

1227 Figure 1. GFED basis regions regrided to the resolution of ModelE2.1 of 2° in latitude by  
 1228 2.5° in longitude.

1229

1230

1231

1232

1233

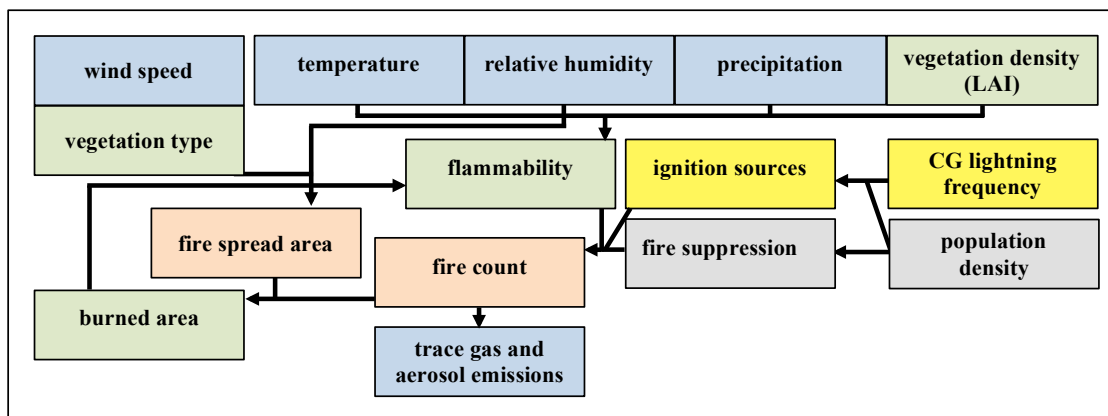
1234

1235

1236

1237

1238



1239

1240

1241 Figure 2. Structure of the fire parameterization of pyrE. Processes related to atmospheric  
 1242 properties in blue, surface properties in green, ignition and suppression in yellow and  
 1243 gray, and fire properties in red.

1244

1245

1246

1247

1248

1249

1250

1251

1252

1253

1254

1255

1256

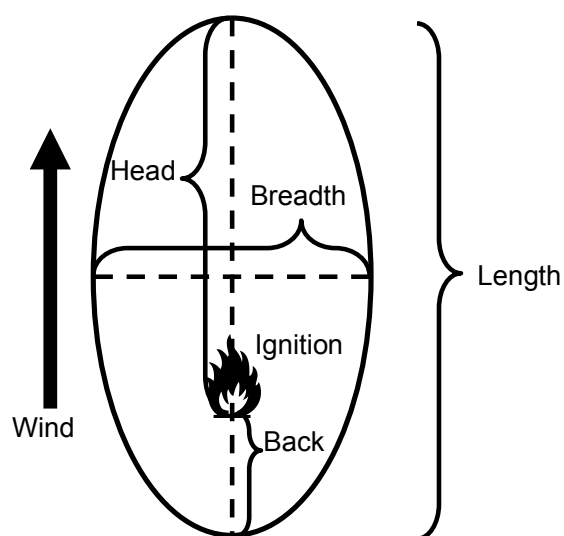
1257

1258

1259

1260



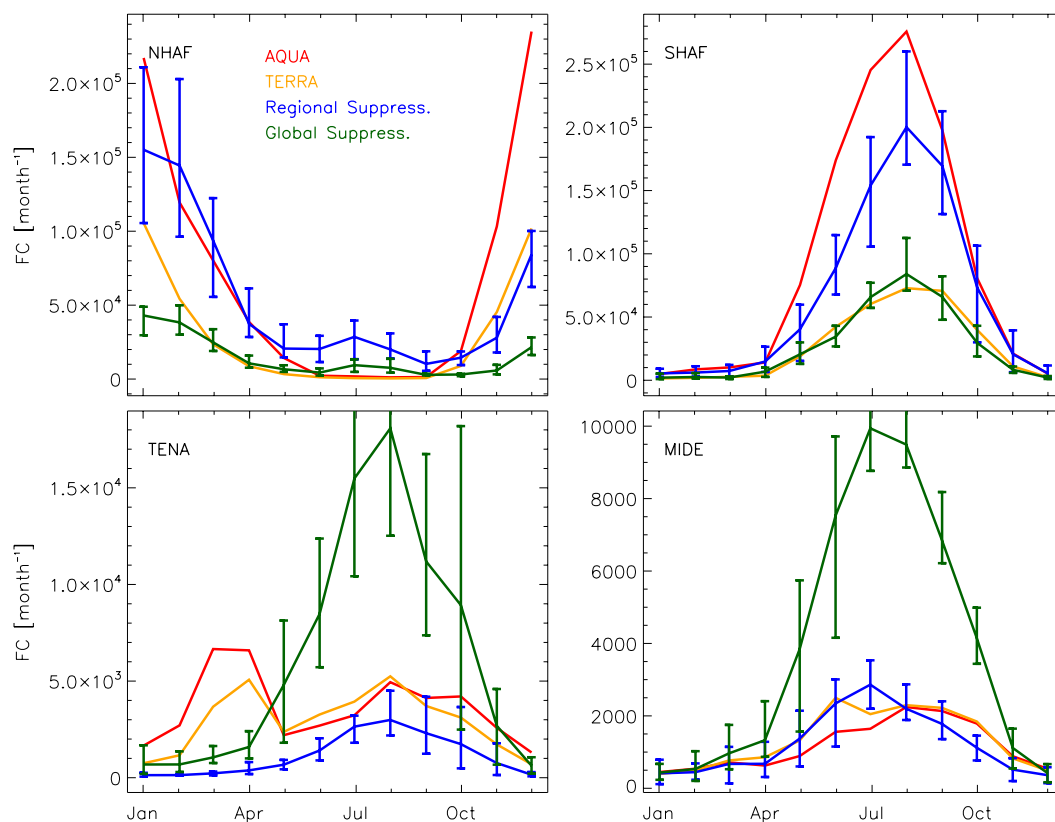


1262

1263

1264 Figure 3. Approximation of a single fire spread. Based on *van Wagner* (1969) and *Arora*  
 1265 *and Boer* (2005).

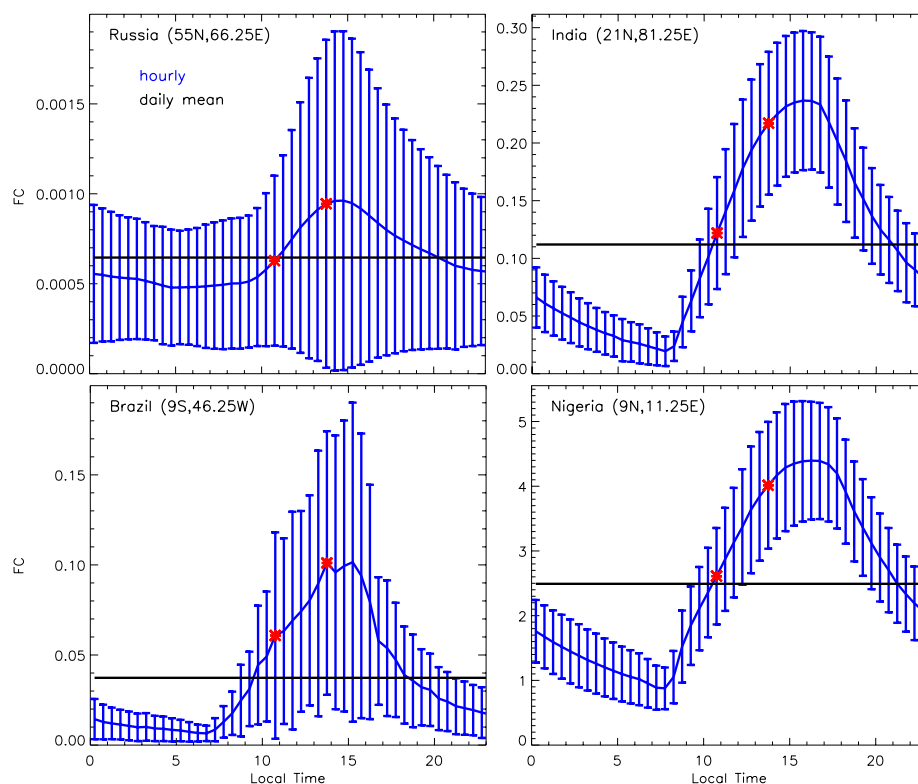
1266



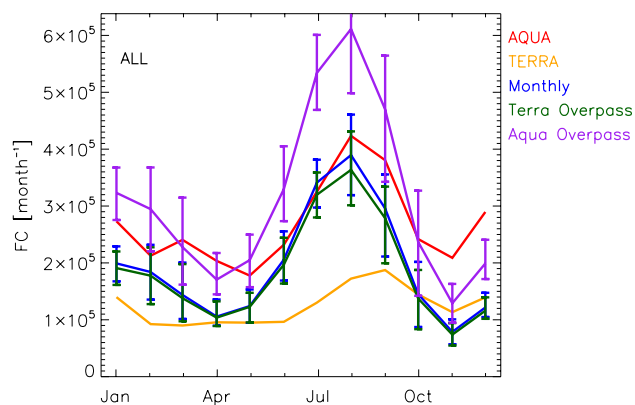
1267

1268 Figure 4: Seasonality of total fire count for NHAF (top left), SHAF (top right), TENA  
 1269 (bottom left) and MIDE (bottom right) observed by MODIS Aqua (red) and Terra  
 1270 (orange) and simulated with explicit regional suppression (blue) and generic global  
 1271 suppression parameterization (green); Eq. 6. Error bars represent the range over 10-year  
 1272 climatological simulations. Note that TERRA and AQUA have different overpass times,  
 1273 and the model data presented here are monthly means. Also, note the different scale in  
 1274 each panel.

1275

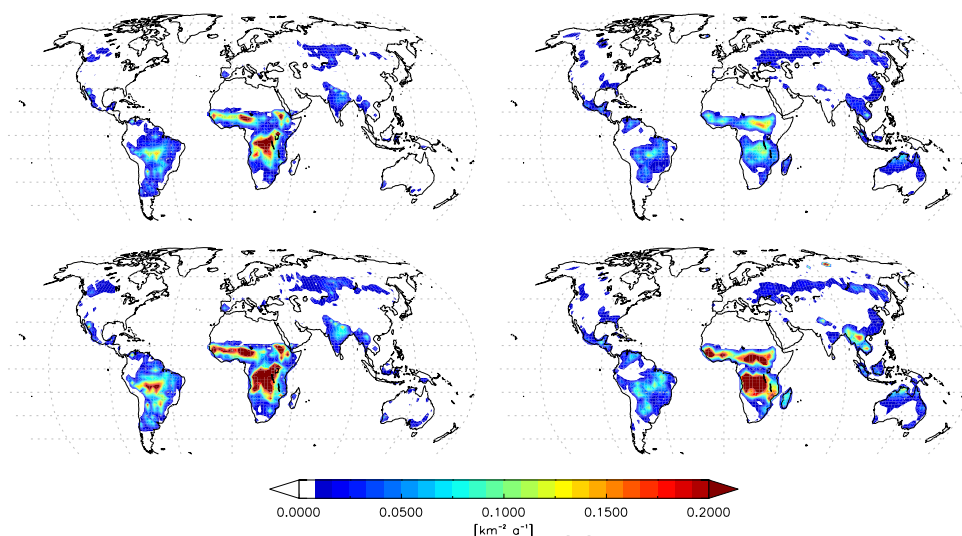


1276  
 1277 Figure 5: Daily mean cycle in fire count (FC, blue line) and daily mean (black line) at 4  
 1278 locations during the month of January. The daytime overpass times of Terra (10:30am)  
 1279 and Aqua (13:30pm) are marked with a red star. Error bars represent the range during the  
 1280 month. Note the different scale in each panel.  
 1281



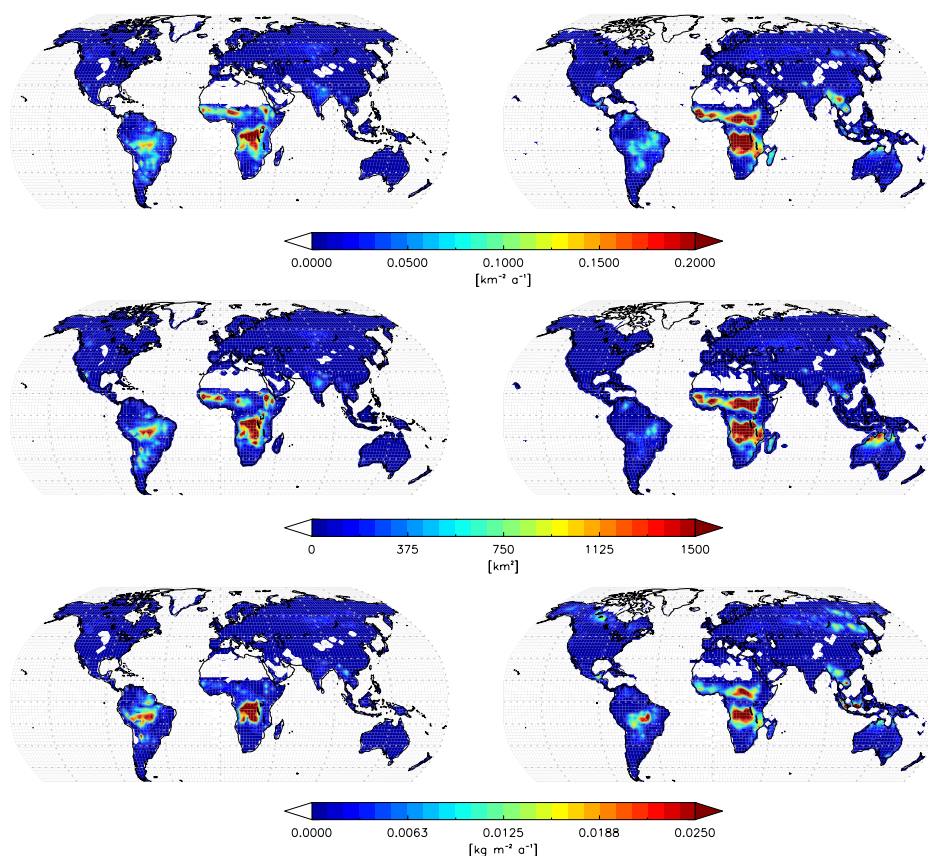
1282  
 1283 Figure 6: Global seasonality of total fire count (FC) by MODIS Aqua (red) and Terra  
 1284 (orange) and simulated by the model: monthly mean (blue), monthly mean sampled at the  
 1285 daytime Terra overpass time (green), and sampled at the daytime Aqua overpass time  
 1286 (purple). Error bars represent the 10-year range in the simulation.

1287  
 1288  
 1289  
 1290  
 1291  
 1292  
 1293



1294

1295 Figure 7: Annual mean model (left) and MODIS (right) fire count. Modeled annual mean  
 1296 is based on an ensemble of 10 simulations. Simulated fires sampled at the daytime Terra  
 1297 overpass time, 10:30am local time (upper left) and daytime Aqua overpass time, 1:30pm  
 1298 local time (lower left). MODIS fire count is based on MODIS Terra (upper right) and  
 1299 MODIS Aqua (lower right) from 2003-2016.



1300  
 1301 Figure 8: Annual mean model (left) and satellite based (right) fire count (upper), burned  
 1302 area (middle), and CO emissions (lower). Modeled annual mean is based on an ensemble  
 1303 of 10 simulations. Satellite detected fire count are based on MODIS Aqua retrievals of  
 1304 2003-2016, burned area is based on GFED4s inventory of 2003-2016, and CO emissions  
 1305 are based on climatological GFED4s emissions of 1995-2010.

1306  
 1307

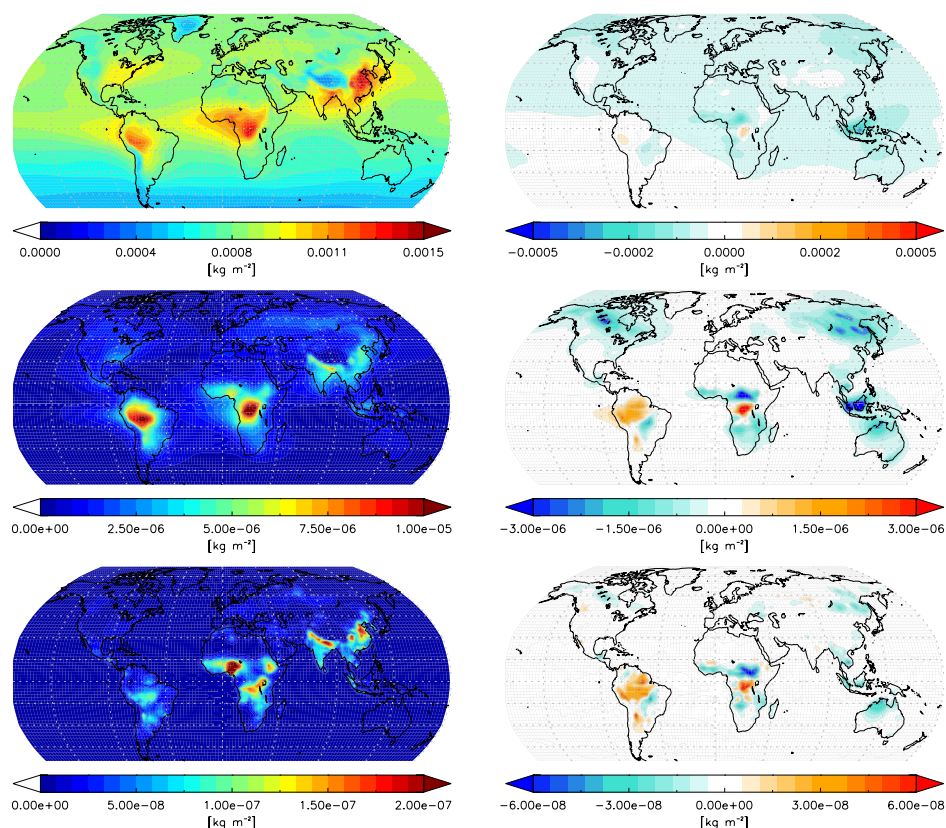
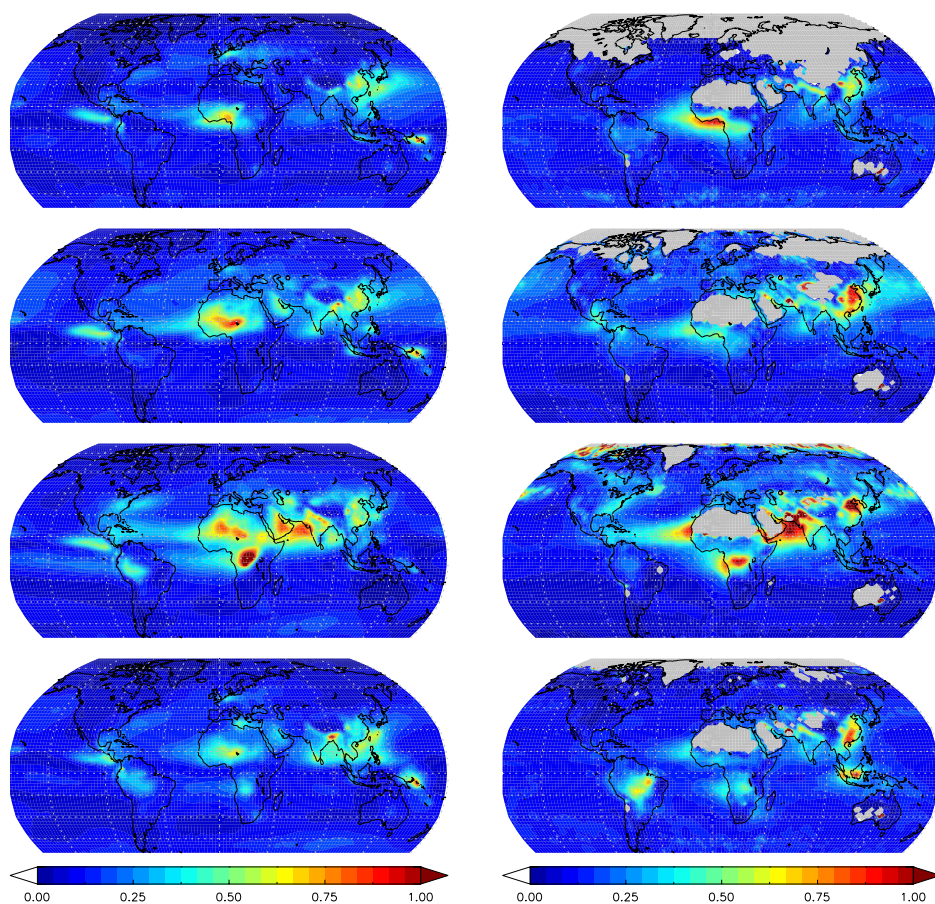


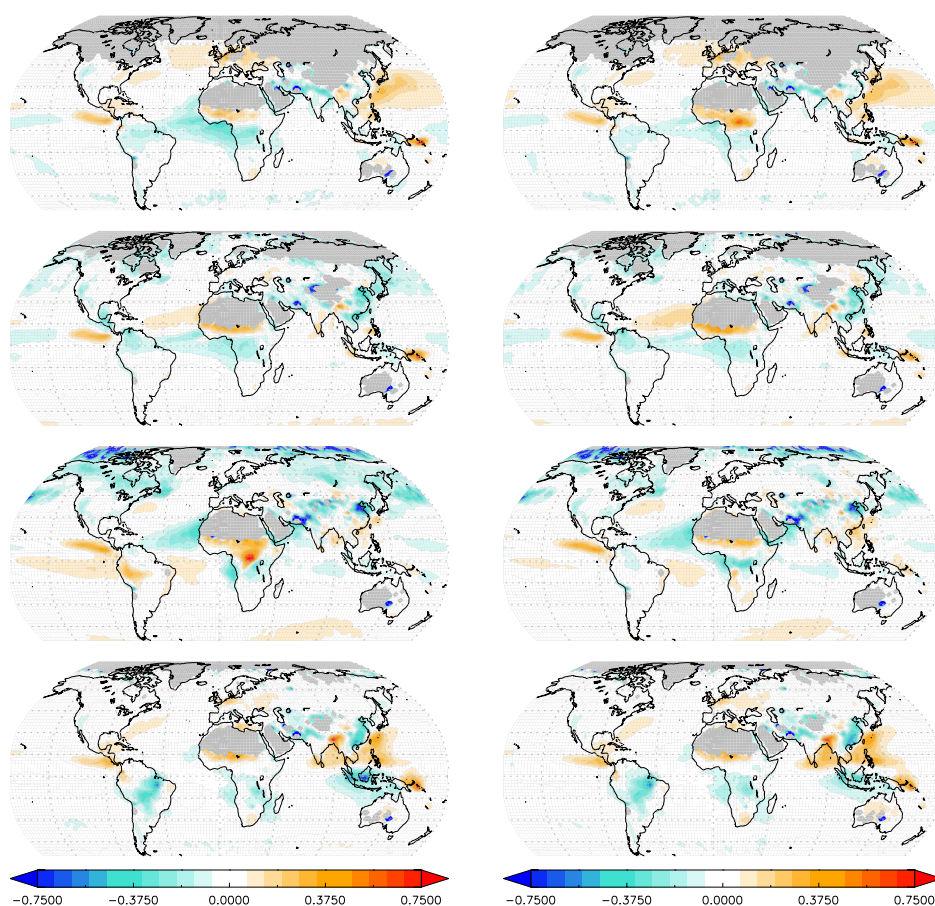
Figure 9: Modeled annual mean column density using pyrE fire emissions (left), and the difference in column densities with a simulation using offline GFED4s emissions (pyrE – GFED4s; right). CO (upper), OA (middle), and BC (lower). Data based on an ensemble of 10 simulations.





1315  
 1316 Figure 10: Monthly modeled clear-sky aerosol optical depth (AOD) simulated using pyrE  
 1317 fire emissions (left), and detected by Aqua-MODIS (right). January (first row), April  
 1318 (second row), July (third row), and October (last row). Monthly mean simulated AOD is  
 1319 based on an ensemble of 10 simulations, and climatologically monthly MODIS AOD is  
 1320 based on 2003-2007 data. Missing MODIS data is shaded in light gray.

1321  
 1322  
 1323  
 1324  
 1325  
 1326



1327

1328 Figure 11: The difference in monthly modeled clear-sky aerosol optical depth (AOD) and  
 1329 MODIS Aqua (model – satellite). Model simulations using pyrE fire emissions (left) and  
 1330 model simulations using offline GFED4s emissions (right). January (first row), April  
 1331 (second row), July (third row), and October (last row). The difference is based on an  
 1332 ensemble of 10 simulations and 2003-2007 MODIS climatological monthly data. Missing  
 1333 MODIS data is shaded in light gray.

1334

1335

1336

1337

1338

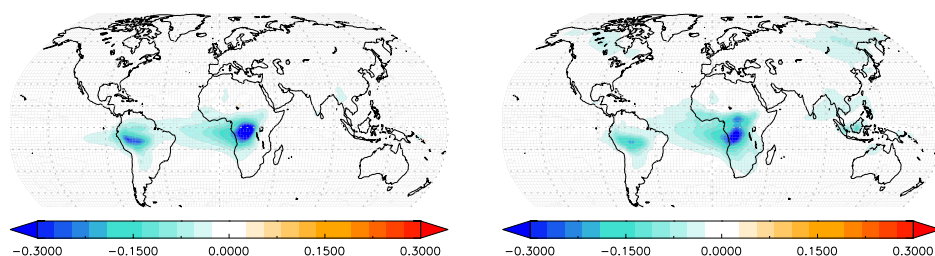
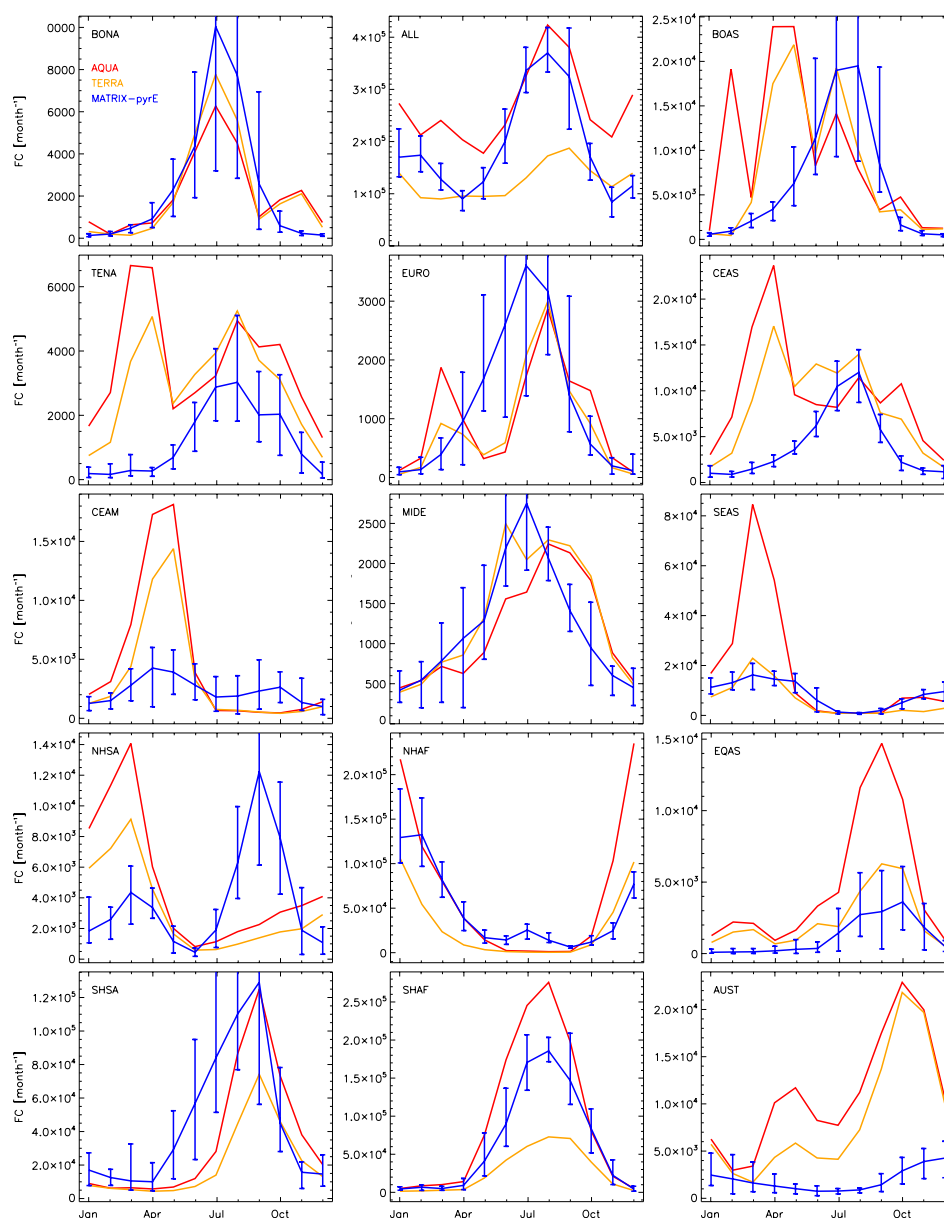


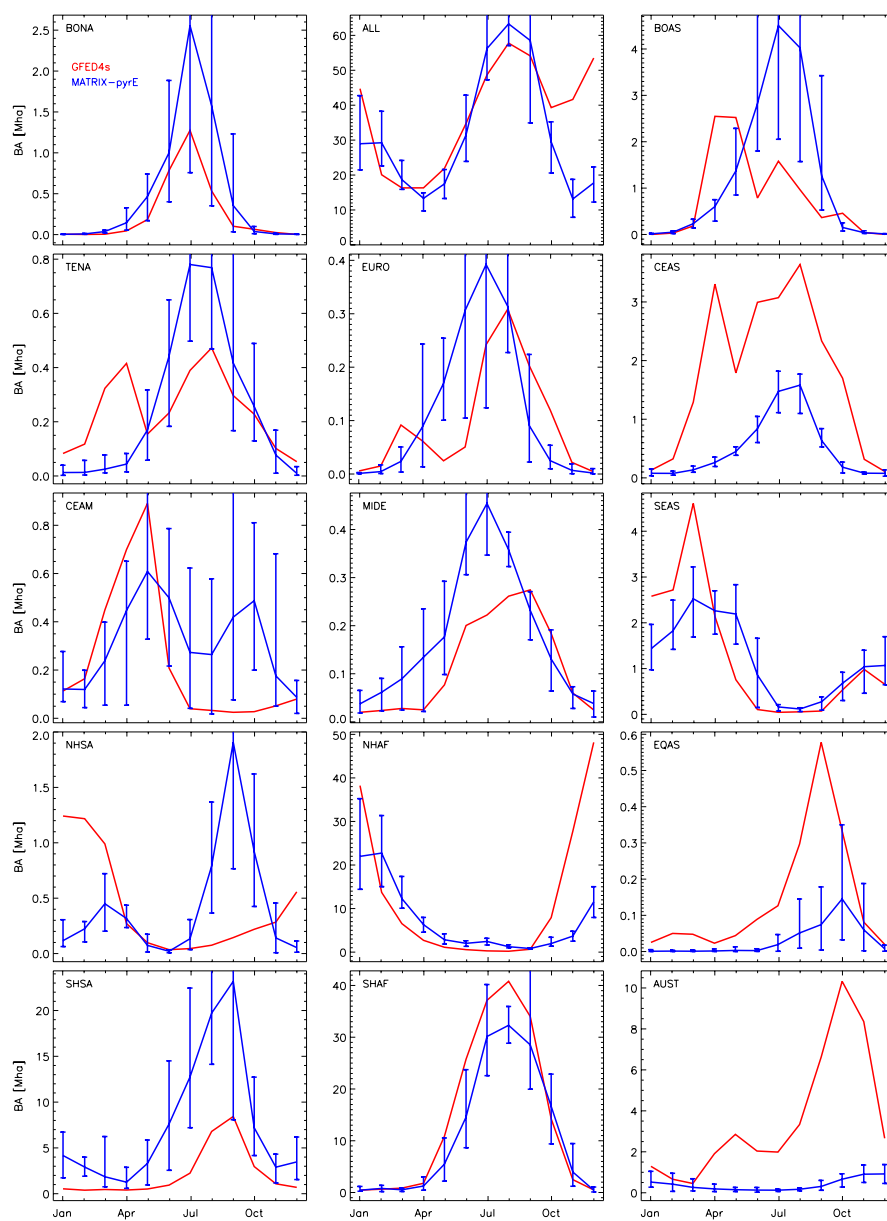
Figure 12: The difference in annual modeled clear-sky aerosol optical depth (AOD) between a simulation with no fire emissions to a simulation using pyrE fire emissions (left), and a simulation with offline GFED4s emissions (right). The difference (model with no fire emissions – model with fire emissions) is based on an ensemble of 10 simulations.



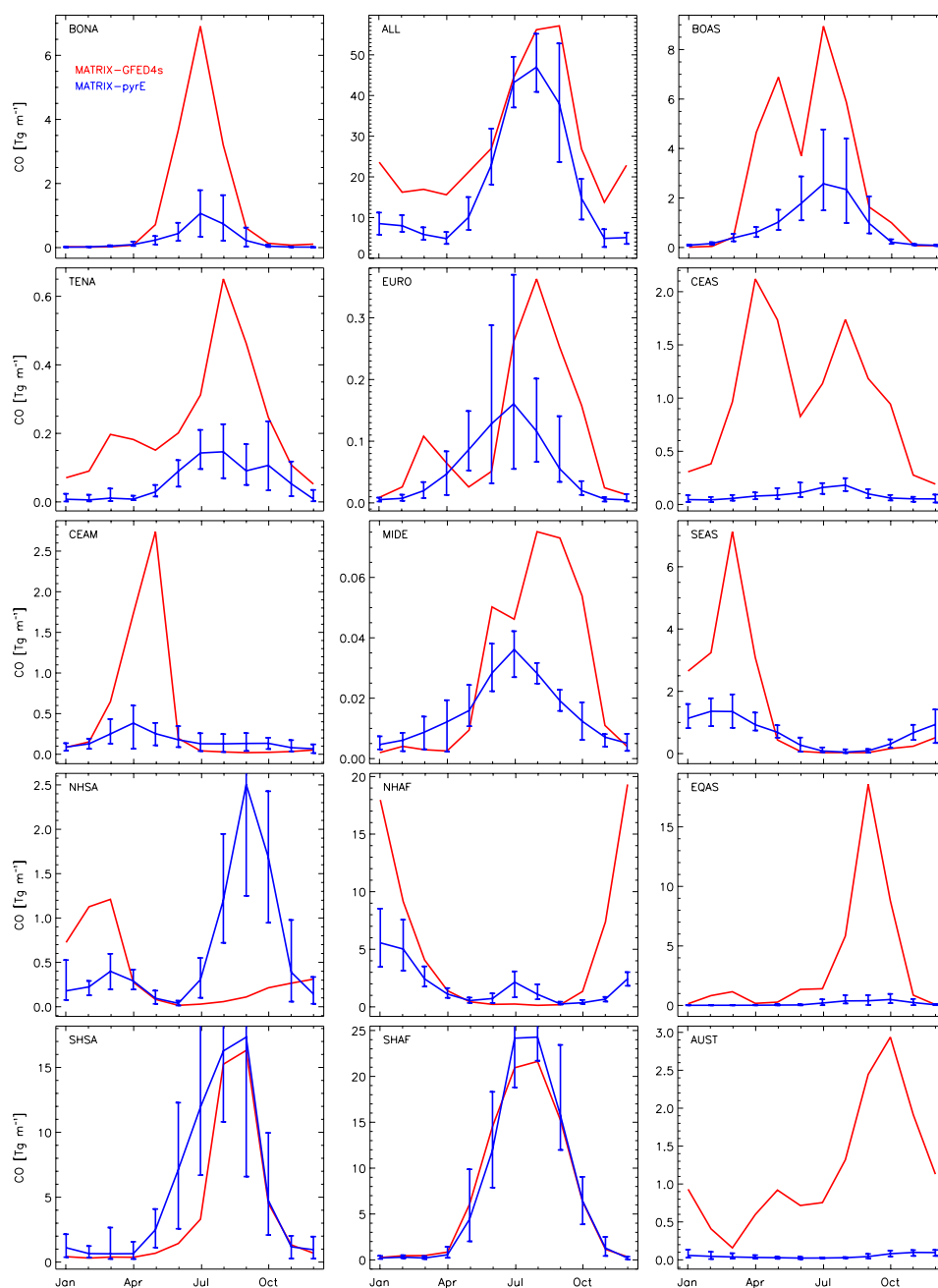
## 1361 APPENDIX



1362  
 1363 Figure A1: Seasonality of total fire count (FC) detected by MODIS Aqua (red) and Terra  
 1364 (orange) and simulated (blue) in all GFED regions (Fig. 1). Error bars represent the 10-  
 1365 year range in the simulations. Note the different scale in each panel.

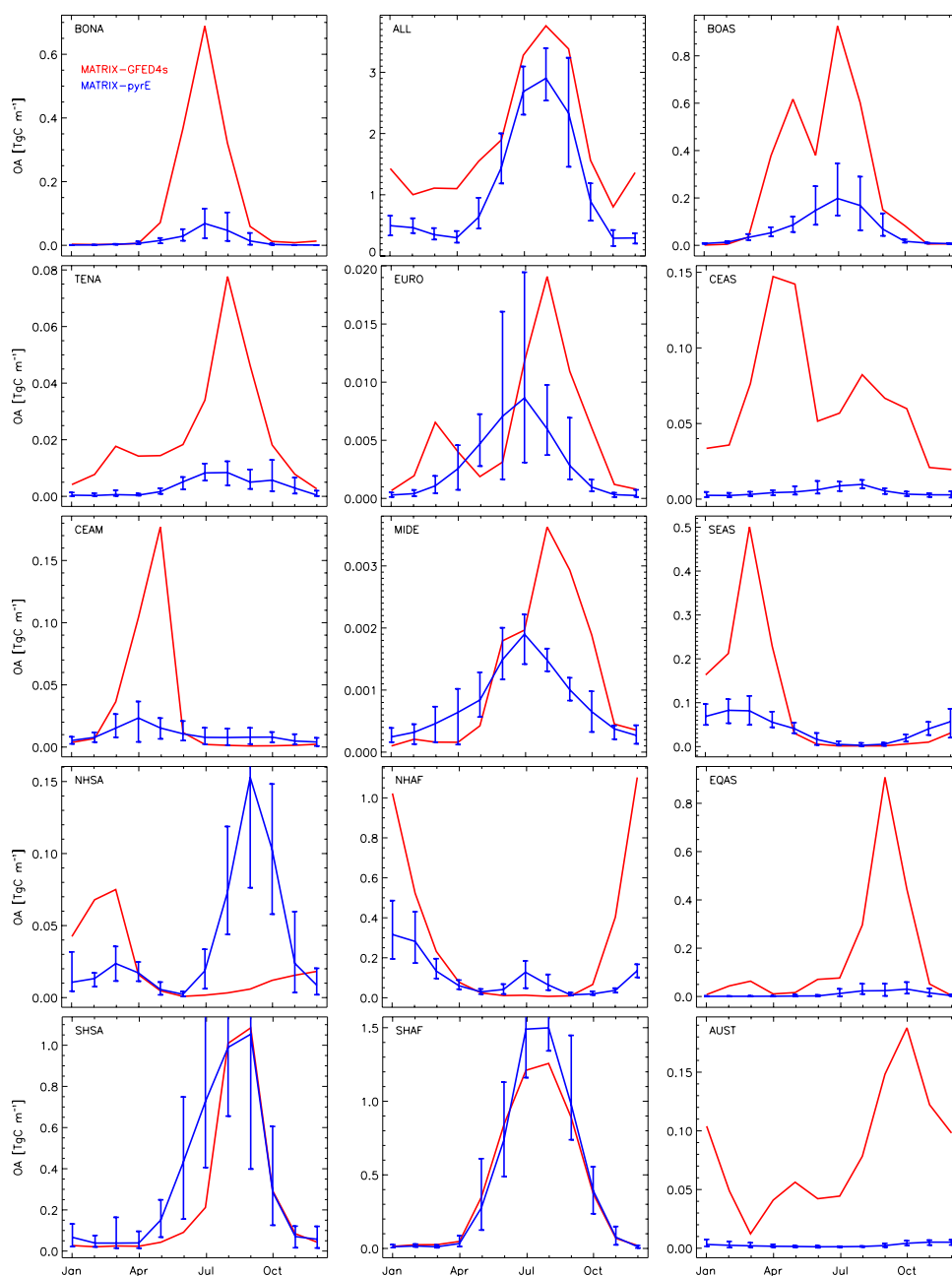


1366  
 1367 Figure A2: Seasonality of total burned area; simulated (blue) and reported by GFED4s  
 1368 (red) in GFED regions. Error bars represent the 10-year range in the simulations. Note the  
 1369 different scale in each panel.



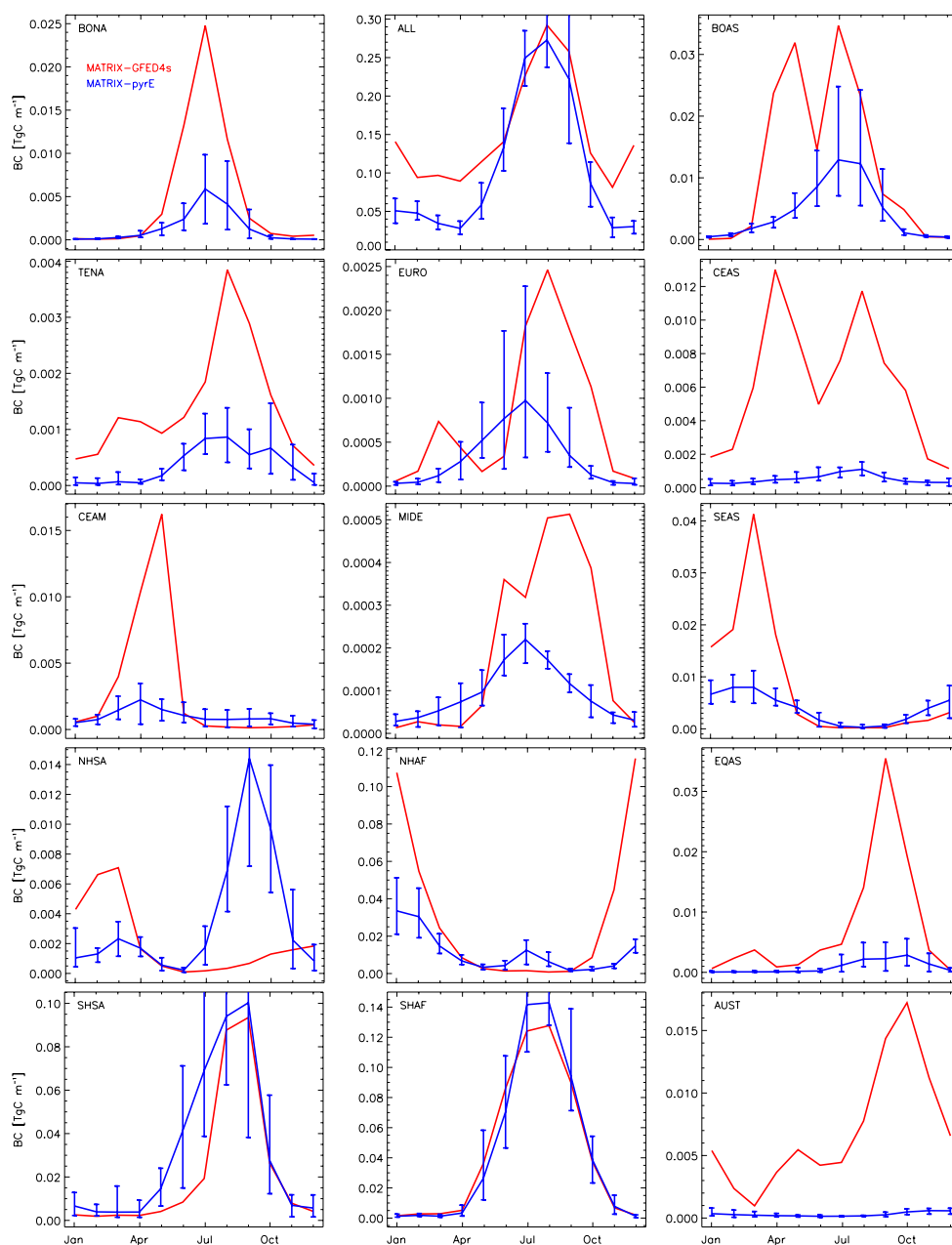
1370  
 1371 Figure A3: Seasonality of total fire CO emissions; simulated (blue) and reported by  
 1372 GFED4s (red) in GFED regions. Error bars represent the 10-year range in the simulations.  
 1373 Note the different scale in each panel.





1374  
 1375 Figure A4: Seasonality of total fire organic aerosol (OA) emissions; simulated (blue) and  
 1376 reported by GFED4s (red) in all GFED regions. Error bars represent the 10-year range in  
 1377 the simulations. Note the different scale in each panel.





1378

1379 Figure A5: Seasonality of total fire BC emissions; simulated (blue) and reported by  
 1380 GFED4s (red) in all GFED regions. Error bars represent the 10-year range in the  
 1381 simulations. Note the different scale in each panel.